CO_2 ACTIVATION ON MnO_x /Pd(111) MODEL CATALYST

A THESIS SUBMITTED TO
THE GRADUATE SCHOOL OF ENGINEERING AND SCIENCE
OF BILKENT UNIVERSITY
IN PARTIAL FULFILLMENT OF THE REQUIREMENTS FOR

THE DEGREE OF
MASTER OF SCIENCE
IN
CHEMISTRY

By
Arca Anıl
July 2022

CO_2 ACTIVATION ON MnO_x/Pd(111) MODEL CATALYST
By Arca Anıl
July 2022

We certify that we have read this thesis and that in our opinion it is fully adequate, in scope and in quality, as a thesis for the degree of Master of Science.

Emrah Özensoy(Advisor)

Oğuz Gülseren

Mehmet Fatih Danışman

Approved for the Graduate School of Engineering and Science:

Orhan Arıkan
Director of the Graduate School

ABSTRACT

CO_2 ACTIVATION ON MnO_x/Pd(111) MODEL CATALYST

Arca Anıl
M.S. in Chemistry
Advisor: Emrah Özensoy
July 2022

CO_2 is an atmospheric pollutant (i.e., a greenhouse gas) and it can be converted into valuable chemicals such as methanol, methane, and formic acid. However, CO_2 reduction is a challenging process due to the thermodynamic stability of CO_2. In this work, we focus on the activation of CO_2 by using an atomically well-defined MnO_x/Pd(111) planar model catalyst. Pd(111) surface can dissociatively adsorb hydrogen molecules, but CO_2 does not strongly bind to the Pd(111) surface. On the other hand, MnO_x nano-structures can facilitate the activation of CO_2 due to the presence of acid and base sites on the metal oxide surface. Therefore, MnO_x/Pd(111) was chosen as a model catalyst to investigate catalytic CO_2 activation. A multifunctional ultra-high vacuum system with quadrupole mass spectrometer (QMS), X-ray photoelectron spectrometer (XPS), and low energy electron diffraction (LEED) was used to perform the experiments. Manganese thin film growth mechanism on Pd(111) surface was determined by using XPS. Manganese was evaporated on Pd(111) substrate at two different temperatures (i.e., 85 K and 300 K). Formation of products after the dosing of the reactants on the MnO_x/Pd(111) surface was examined via temperature programmed desorption (TPD). For both cases, formed manganese oxide thin film was investigated by using XPS to estimate the relative, Mn^0, Mn^{2+} and Mn^{3+} surface concentrations. Prepared manganese film on Pd(111) at 300 K could activate CO_2 to CO, which is a valuable chemical for the chemical industry. To prepare smaller clusters, manganese was evaporated on the Pd(111) single crystal surface at 85 K. At moderate manganese coverage, carbonate CO_3^{2-} formation was detected on the MnO_x/Pd(111) interfacial sites.

Keywords: Activation, Pd(111).

ÖZET

MnO_x/Pd(111) MODEL KATALİZÖRÜNDE CO_2 AKTİVASYONU

Arca Anıl
Kimya Bölümü, Yüksek Lisans
Tez Danışmanı Emrah Özensoy
Temmuz 2022

CO_2, hem bir atmosferik bir kirletici hem de bir sera gazıdır ve bu bileşik daha değerli olan metanol, metan ve formik asit gibi ürünlere dönüştürülebilir. Ancak, CO_2 molekülünün yüksek termodinamik kararlılığı nedeniyle indirgenmesi zordur. Biz bu çalışmada, MnO_x/Pd(111) düzelmsel model katalizörü üzerinde, CO_2 aktivasyonuna odaklandık. Pd(111) yüzeyi, hidrojen molekülünü parçalayarak, kendi yüzeyine yapıştırabilmekte, fakat CO_2 molekülünü kendi yüzeyine kuvvetli bir biçimde bağlayamamaktadır. MnO_x nano-yapılarının, asidik ve bazik yüzey sitelerine sahip olmaları nedeniyle, CO_2 molekülünün aktivasyonunda, kolaylaştırıcı bir rol aldıkları bilinmektedir. Mevcut çalışmadaki deneyler, ultra yüksek vakum sisteminde bulunan dört kutuplu kütle spektrometresi (QMS), X-ışını spektrometresi (XPS), düşük enerjili elektron kırılımı (LEED) cihazları kullanılarak yapılmıştır. Mangan'nın Pd(111) yüzeyindeki, ince film büyüme mekanizması, XPS kullanılarak incelenmiştir. Mangan, iki farklı sıcaklıkta (85 K ve 300 K) Pd(111) yüzeyine buharlaştırılmıştır. Reaktantların dozlanmasından sonra, ürünlerin oluşumu sıcaklık programlı yüzey salınımı (TPD) ile incelenmiştir. Her iki durum için de Mn^0, Mn^{2+} ve Mn^{3+} konsantrasyonu XPS kullanılarak belirlenmiştir. Oda sıcaklığında hazırlanmış filmler, endüstride değerli bir molekül olan CO'i, CO_2 den elde edebilmiştir. Daha küçük MnO_x parçacıkları hazırlayabilmek için, Mn buharlaştırılması, Pd(111) yüzeyine 85 K'de yapılmıştır. Ortalama mangan film kalınlığında, karbonat CO_3^{2-} oluşumunu, MnO_x/Pd(111)(yüzeyinde gözlemlenmiştir

Anahtar sözcükler: Aktivasyon, Pd(111).

Acknowledgement

I must stress that I was not unaccompanied during the two years that I continued this project and it takes a village to carry out a project such as this one. The feeling of blessing is the product of the great times I spent with those around me throughout my master's degree and I would like to thank all of my professors for their contributions throughout my undergraduate and graduate studies.

I am very thankful for my advisor Emrah Özensoy, without Prof. Özensoy, this project would not exist furthermore I'd not have acquired the necessary knowledge for me to succeed academically. Likewise, I'd like to express my deepest thanks to Igor Lyubinetsky for his patience. Everything I learned about the project came about as a result of his efforts. It is necessary to be very lucky to find a mentor whose energy matches mine, and thanks to this, we were able to achieve a peaceful lab environment. I would also like to thank Yusuf Koçak, with whom I worked side by side and who took time for me whenever "Asuman" had problems. Moreover, I am grateful for Bartu Karakurt who helped me from Europe when I got stuck.

I cannot begin to express my thanks to Ömer Faruk Sadak, who was not merely a lab partner. No matter how hard times "Asuman" gave us, you never let us give up and when I was overworked, you were the one who told me to take a breather to reset my fuming head. You are an irreplaceable buddy of mine and I am almost certain that it would be impossible to find a friend that I can have this many inner jokes with. Remember, B, pretend as nothing happened.

I'd also like to express my gratitude to Salim Can Akyürek, Beyza Erdivan, Gözde Karaoğlu, Ayşe Dilay Erdalı, Ahsan T. Jalal. The most special thanks to Yağmur Altınkaynak who is my favorite coffee and chat company, you will be greatly missed, my friend. I'd also like to thank Gökberk Katırcı, I wish we could have done more guitar sessions.

I could not have undertaken this journey without Eylül Ergün. I also want to thank her for always supporting me in my stressful, depressed times and showing me the way out. I hope our paths don't stay apart for a long time.

My designated psychologist, Burak Tezcan, thank you for the "therapy" sessions

after a tiring workday. Additionally, I'd also like to acknowledge the help of Bartu Yaman and Mertkan for introducing me to the chemistry industry.
Finally, I'd like to extend my deepest gratitude to my biggest supporters and my dear family, Oya Anıl, Mehmet Anıl, Deniz Anıl, and Mustafa "Mıstık" Dolgun. Thanks to your unparalleled guidance, I have come to these days, you are the biggest source of my success. Thank you for your unending support, love, and patience.

Contents

List of Figures

List of Tables

Chapter 1

Introduction

1.1 Carbon Dioxide as Energy Source

Energy is one of the most important global problems. One sustainable solution is the reduction of carbon dioxide. Reduction of the carbon dioxide can form methanol and ethanol, which are more valuable chemicals than CO_2 as they can be used as fuels [15, 16]. Unlike conventional fossil fuels, methanol and ethanol are more environmental friendly energy sources. Moreover, the energy density of ethanol and methanol is also reasonably high (Table 1).

Fuel Name	Energy Density (MJ/kg)	Specific Energy
Methanol	22	4.4
Ethanol	27	23.2
Diesel	12.6	10.6
Gasoline	46	33.86
Coal	8.2	7.6
Wood	4.2	3.0

Table 1.1: Energy density and specific energy of some fuels. Adapted from Ref. [13, 14]

Another essential problem is the increasing carbon dioxide emissions to the atmosphere. Therefore, converting carbon dioxide to valuable chemicals is an essential process. Under high pressures, carbon dioxide reduction to methanol, ethanol, and other valuable chemicals is possible with a proper catalyst [17, 18, 19].

1.2 Literature Review of CO_2 Hydrogenation

Hydrogenation of CO_2 into valuable compounds such as alcohols is crucial because it not only reduces the greenhouse gas emission caused by CO_2, but also allows CO_2 to be converted into C1 building blocks [20, 21, 22]. Catalytic methanol synthesis via hydrogenation of CO_2 received significant attention [23]. Different reaction mechanistic pathways can synthesize methanol from CO_2. Some of these pathways include formate, hydroxyl, and CO species and may involve reverse water-gas shift (RWGS) reaction [24]. In the formate path, CO_2 is first reduced to HCOO and then further reduced to methanol on the bimetallic catalyst. For instance, according to theoretical calculations, methanol synthesis on Pd-Cu alloy is possible, which was achieved under high pressures (> 50 atm) [25, 26]. Moreover, $Pd/Mn-TiO_2$ catalyst produces ethanol from CO_2 under high pressure (> 50 atm), temperature (> 400 K), and UV radiation [27].

As shown in Figure 1.1, activation of the CO_2 molecule O-C-O bond angle may change, C-O bond length may elongate, and the C-O bond polarization may be altered [1]. CO_2 activation is represented in Figure 1.1.

Bending of O-C-O angle may occur when CO_2 is adsorbed on transition metal surfaces. The bending occurs due to the electronic interaction between the molecule and the metal [28]. There are nine possible different coordination types with which CO_2 molecule can coordinate to metal site. For each coordination type, a particular Walsh Diagram can be drawn, and molecular energies with respect to the angle between the oxygen atoms in the CO_2 molecule can be calculated theoretically.

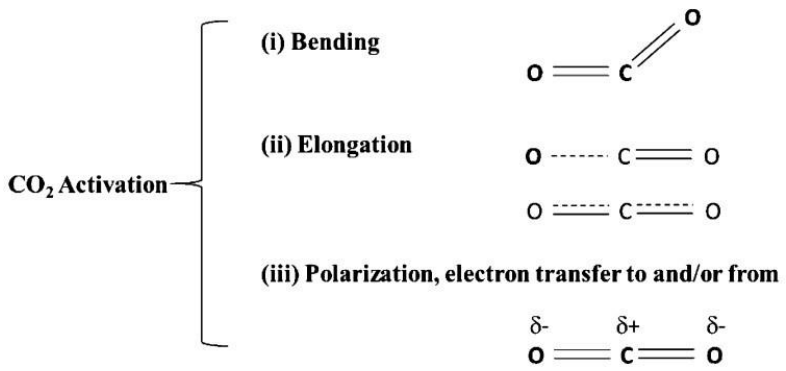

Figure 1.1: Configurational changes that may occur during CO_2 activation. Adapted from Ref. [1].

CO_2 molecule has 16 valence electrons in the molecular orbitals, which are distributed among the carbon and oxygen atoms. The carbon atom in the carbon dioxide molecule shows an electrophilic character, which is an exception for the overall energetics of the molecule. While nucleophilic reactions occur on the carbon side, electrophilic reactions are observed on the oxygen side. This means that both nucleophilic and electrophilic reactions are possible for the carbon dioxide molecule. For instance, water, which is a nucleophilic molecule, can attack the electrophilic carbon center of the carbon dioxide. Moreover, the CO_2 molecule's carbon side can get electrons from the metallic catalyst surface. The oxygen side can donate the electrons due to the nucleophilic character[29].

CO_2 activation is feasible at relatively high temperatures (> 400 K), which makes the RWGS reaction more feasible [16].]. Secondly, at high temperatures (> 600 K), the aging of catalysts is another problem, which can lead to the degradation of the catalytic performance. Cu, Zn, Cr, and Pd are leading catalytic metals for maximizing methanol production and selectivity while minimizing the generation of undesirable by-products such as other hydrocarbons in CO_2 reduction [30].

On the other hand, bimetallic catalysts can reduce carbon dioxide under high pressures (> 50 atm). For instance, Cu-Ni, Cu-Zn, and Cu-Pd are effective catalysts that can reduce CO_2 to methanol under high pressures [25]. Moreover, electrochemical CO_2 activation is also possible on $Ag_{76}Sn_{240}$, Cu – Sn, and Au – Pt catalysts [31, 32, 33]. CO is also a possible product during the CO_2 reduction

reactions. Although CO is a more toxic and dangerous molecule than carbon dioxide, it is an important reactant to produce other chemicals in the chemical industry. CO and H_2 gas mixtures are called syngas. By using syn-gas, methane, dimethyl ether, methanol, and ethanol, production is possible in the chemical industry [34, 35, 36]

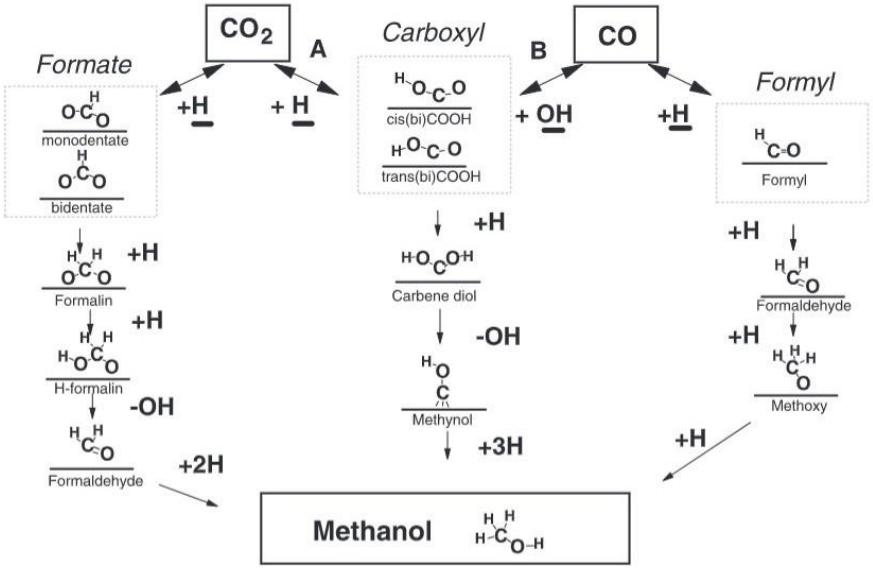

Figure 1.2: Reaction mechanism of the methanol formation from CO_2 Adapted from Ref. [2]

One of the possible products that can be obtained from CO_2 reduction is methanol (Figure 1.2). However, many intermediates and different reaction mechanisms for the methanol formation are achievable with reduction of the CO_2. For instance, according to the DFT calculations, there are three main pathways for the CO_2 reduction [23]. These are formate (CHOO), carboxyl (HOCO), and formyl (HCO) reaction pathways. In the formate pathway, CO_2 molecule re- acts with a proton, and the formate molecule occurs on the surface, which can be adsorbed as monodentate or bidentate. Following hydrogenation of the formate, formalin ($OOCH_2$), H-formalin ($HOCH_2O$, formaldehyde (H_2CO) and finally methanol molecule occurs. In the carboxy pathway, CO_2 takes a proton

and cis or trans carboxyl forms. Hydrogenation of the molecule causes to occur carbene diol (HOCOH). Due to the leaving of the -OH, methanol (HOC-) intermediate is formed, and finally, protonation of this intermediate gives rise to form of methanol. In the formyl path, carboxyl molecule, which occurred due to hydrogenation of the CO_2 molecule, loses the -OH group, and CO molecule are produced. Protonation of the CO molecule forms the formyl (HCO). Hydrogenation of the formyl gives rise to formaldehyde (OCH_2) and methoxy (– OCH_3). Finally, methoxy takes hydrogen, and methanol forms [2]. Methanol formation reaction pathway can be seen in Figure 1.2.

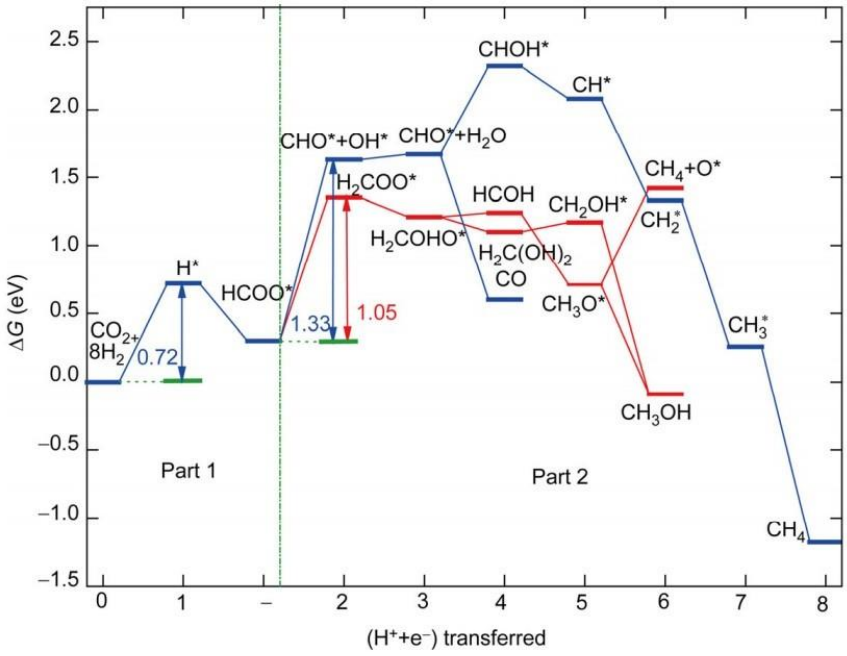

Figure 1.3: Free energy diagram of CO_2 reduction on Pb(211) surface. The blue line shows pathway 1, and the red line shows pathway 2. Adapted from Ref. [3].

Another possible product that can be obtained from the CO_2 reduction is methane (CH_4). Mo doped hexagonal $WO_3 \cdot 0.33\,H_2O$ photocatalyst can produce methane from CO_2 [37]. The mechanism of the CO_2 reduction to methane has more than one pathway. However, all the reactions begin with the adsorption of the CO_2 molecule. According to a DFT study on the Pb(211) surface, firstly CO_2 takes a proton and HCOO* species [3] which can convert into CHO* and CHO · +

$OH\cdot$ after hydrogenation of the CHO* intermediate. Upon the departure of the oxygen atom, CH_4 can form with further hydrogenation. (Figure 1.3)

Selectivity of the catalyst is another important catalytic property since CO_2 reduction reaction can yield more than one product. For instance, InO_2 catalyst has a high methanol selectivity[38]. However, the aging of the InO_2 catalyst decreases the selectivity due to its changing of the surface. The selectivity of the catalyst and surface are related to each other because intermediates intract with the d-band of the metal [39]. Moreover, the presence other molecules in the catalytic environment can affect selectivity. For instance, electrochemical reduction of the carbon dioxide on the copper catalyst favors methane at high bicarbonate concentrations, while low $KHCO_3$ concentrations increase ethylene selectivity [40].

According to DFT studies, Pd bimetallic surfaces are one of the most active catalysts for reducing CO_2 [26, 41, 42]. Palladium metal oxide catalysts are also capable of reducing CO_2 [43]. In the literature MnO_x nanoparticles can activate the CO_2 [44, 45, 5] Therefore, in the current work, by using temperature programmed desorption (TPD) and x-ray photoelectron spectroscopy (XPS), we investigated the interaction of CO_2 with a heterogeneous bi-component model catalyst made up of MnO_x clusters supported on a Pd(111) surface under ultra-high vacuum (UHV) conditions.

1.3 Model Heterogeneous Catalysts Under Ultra-High Vacuum Conditions

Under ultra-high vacuum (UHV) conditions, controlling the surface properties of catalytic materials is possible. Chemical composition, particle size, morphology, and crystal structure can be determined by various spectroscopic techniques. The main advantage of the utilization of model catalysts is to control the complex morphology and chemical features, which is rather challenging for real catalysts consisting of various metals and metal oxides operating under high pressures [5].

1.4 Crystal Structures

Face-centered cubic (fcc), body-centered cubic (bcc), and hexagonal close-packed (hcp) crystal structures are the three most common crystal structures for bulk metals. While some transition metals and alkali metals crystallize in bcc structure, the majority of metals prefer to stack in the fcc or hcp systems. Groups VIII and I-B are the most commonly used active sites in catalysis (e.g., fcc: Ni, Cu, Rh, Pd, Ag, Ir, Pt, Au, hcp: Co, Ru, Os, and bcc: Ni, Cu, Rh, Pd, Ag, Ir, Pt, Au), If the lattices are considered to be made of tightly packed spherical atoms, fcc, and hcp lattices have high density, with roughly 26% unoccupied space. Each atom in the interior has 12 nearest neighbors, or in other words, a coordination number of 12. The bcc lattice is slightly more open, with approximately 32% vacant space. A bulk atom's coordination number inside the bcc lattice is 8. Various planes on fcc, bcc, and hcp structures are represented by the miller indices [9]. Most commonly utilized planes for the fcc crystals in model catalyst studies are (111), (110) and (100) (Figure 1.7).

Detailed reaction mechanisms on single crystals can be readily studied under ultra-high vacuum conditions since, under high pressures, surface reconstruction

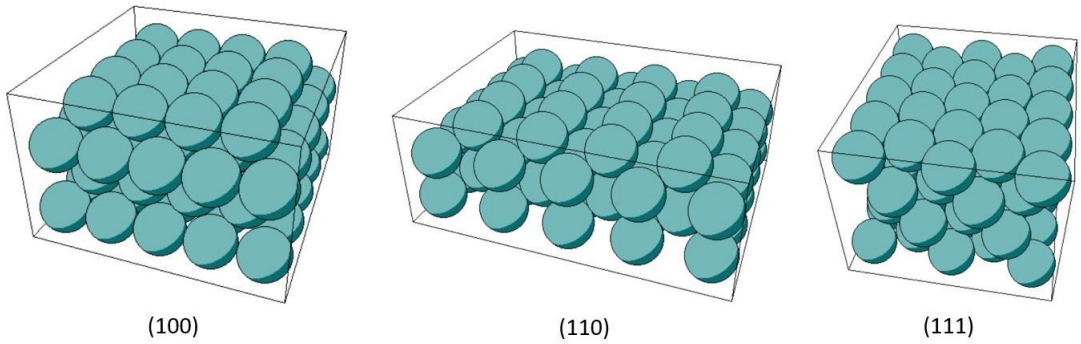

Figure 1.4: Fcc (100), (110), and (111) surfaces.

and adsorption of unwanted molecules may occur [46, 47]. For instance, Au single crystal surfaces may undergo spontaneous reconstruction under ultra-high vacuum conditions [48, 49, 50]. Furthermore, strongly adsorbed molecules can also induce surface reconstruction of the surface. In addition, Cu(111) and Cu(110) surfaces can undergo reconstruction upon oxygen adsorption, which was observed by ion scattering experiments [51]. Surface-free energy, which is the required energy to create a surface, also varies with respect to the planes. For instance for Pd(111), Pd(110) and Pd(100) surface free energy is 1.920, 2.326 and 2.225 J/m^2 respectively[9].

1.5 Reactions on Surfaces

In heterogeneous catalysis, reactions on the surfaces begins with the adsorption of at least one of the reactants. There are two types of adsorption phenomena of the reactants on the planar surfaces, which are called physisorption, and chemisorption. Physisorption is the physical bonding of the gas molecules to the solid surface due to the Van der Waals forces, thus it is a weak interaction between the adsorbate and adsorbent (10 - 30 kJ/mol) [52]. On the other hand, chemisorption occurs due to the chemical bond between adsorbate and surface, thus causes stronger adsorption (bigger than 80 kJ/mol) than physisorption. The crystallographic structure of the adsorbed overlayers can be determined via diffraction techniques, such as LEED [53].

After the adsorption of A, another reactant, B, can be adsorbed on the surface. Then, adsorbed A and B can react and form the adsorbed molecule C*. In the last step of the reaction, adsorbed molecule, C*, desorbs from the surface. This reaction is called as Lindemann Hinshelwood mechanism, as shown in Eqn. (1.1, 1.2, 1.3 and 1.4) below.

$$A_{(g)} \longrightarrow A^* \tag{1.1}$$

$$B_{(g)} \longrightarrow B^* \tag{1.2}$$

$$A^* + B^* \longrightarrow C^* \tag{1.3}$$

$$C^* \longrightarrow C_{(g)} \tag{1.4}$$

Another reaction mechanism in heterogeneous catalysis is the Eley-Rideal mechanism, which is not a common reaction occurring on the surface. Eley-Rideal reactions begin with the adsorption of one of the gas molecules (e.g., A). Adsorbed molecule reacts with another gas molecule B. (the surface does not adsorb B) Eley-Rideal mechanism is represented in Eqn. (1.5, 1.6 and 1.7) below.

$$A_{(g)} \longrightarrow A^* \tag{1.5}$$

$$A^* + B_{(g)} \longrightarrow C^* \tag{1.6}$$

$$C^* \longrightarrow C_{(g)} \tag{1.7}$$

Lindemann Hinshelwood mechanism is a more commonly observed reaction mechanism than Eley-Rideal reaction mechanism [54].

1.6 MnO_x /Pd(111) Catalyst for CO_2 Activation

Palladium has a face-centered cubic (fcc) structure which has a lattice parameter of 0.389 nm at 298 K[55, 56]. Additionally, palladium has several unique properties that allow it to be used in a wide range of hydrogen technologies since palladium has the ability to absorb large volumes of hydrogen at room temperature and under atmospheric pressure, forming palladium hydride in the process

PdH_x [57]. Although bulk palladium can absorb large amounts of hydrogen, hydrogen prefers to be on the surface rather than in bulk under UHV conditions and at low temperatures such as < 300 K [58]. Low Energy Electron Diffraction experiments show that hydrogen atoms adsorbed on Pd(111) single crystal in the $(\sqrt{3}x\sqrt{3})$xR30° orientation at 2/3 monolayer (ML) hydrogen coverage [59]. Dissociatively adsorbed hydrogen has a second-order desorption mechanism. There are repulsive forces between adsorbed hydrogen atoms on the palladium surface, so desorption temperature depends on the hydrogen coverage.

Adsorption sites on the fcc(111) surface include hollow, bridging, and linear adsorption sites, which can be seen in Figure 1.5.

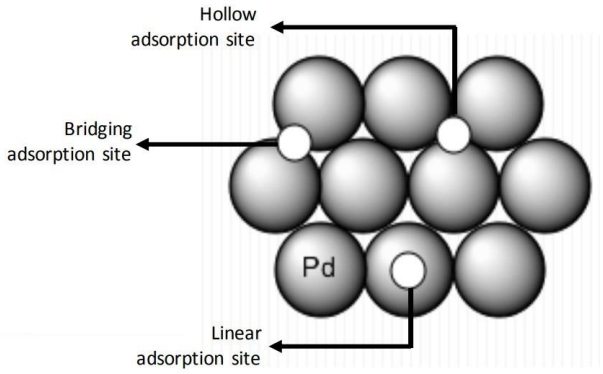

Figure 1.5: Typical adsorption sites on a fcc(111) surface. Adapted from Ref. [4].

CO chemisorbs on Pd(111) thus removing CO from the sample is not an easy process. At 2/3 ML coverage, CO forms an overlayer on Pd(111) with a $(\sqrt{3}x\sqrt{3})$xR30° structure [60]. At various CO coverages, one-fold, two-fold, and three-fold CO adsorption is observed on Pd(111) (Figure 1.6) due to the repulsive interaction among the CO molecules. Adsorption geometry of the CO molecule can be determined via not only LEED but also infrared reflection-adsorption spectroscopy (IRAS) due to the vibrational coupling of CO-CO (that causes the borrowing of the IR intensity) and electron back donation, which changes with

the CO adsorption geometry. Therefore, CO stretching frequencies change with respect to the CO coverages on Pd(111) surface. For instance, electron back donation is weaker for an on-top site than that of a bridge site [61].

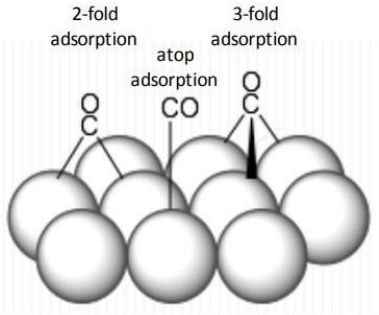

Figure 1.6: Typical CO adsorption geometries on the Pd(111) surface. Adapted from Ref. [4].

The catalyst lifespan can be affected by the extent of CO adsorption on the active sites of the Pd(111) surface [62, 63]. CO overlayer structure on the Pd(111) surface at a 0.6 ML coverage can be seen in Figure 1.7.

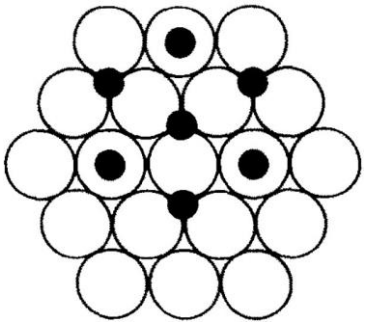

Figure 1.7: CO adsorption structure on the Pd(111) single crystal surface at a 0.6 monolayer coverage. Adapted from Ref. [5].

To reduce the CO_2, adsorption of the molecule on the surface of the catalyst is crucial. Although hydrogen dissociatively adsorbs on Pd(111) surface, CO_2 is weakly adsorbed on the Pd(111) surface, and activation of the CO_2 is not observed [64, 65]. On the other hand, some bi-component catalysts such as copper (Cu), nickel (Ni), rhodium (Rh) with a metal oxide support are capable of CO_2 reduction to produce methanol, methane and formic acid [66, 67, 68, 69]. Therefore, choosing a suitable oxide component with complementary chemical

properties can facilitate the CO_2 reduction process [70]. While the majority of research on metal-oxide systems concentrates on the metal particles dispersed on the oxide support, oxide particles supported on the metal have received comparatively little attention. The size of the metal oxide particles on the metal surface is also very crucial to activating CO_2 molecules. MnO_x nanoparticles that can facilitate the C_5^+ hydrocarbons generate a significant motivation to work on a MnO_x /Pd(111) planer model catalyst to activate carbon dioxide.

In this study, CO_2 activation process was examined on a MnO_x/Pd(111) model catalyst under ultra-high vacuum conditions by utilizing the TPD method. Particularly, we examined the oxidation state of MnO_x overlayers formed at room temperature and 85 K on the Pd(111) surface via XPS.

Chapter 2

Experimental Methods

2.1 Ultra-High Vacuum Experimental Set-Up

Custom-made multifunctional UHV system used in the current work (Figure 2.6) is equipped with X-ray photoemission spectroscopy (XPS), temperature programmed desorption spectroscopy (TPD)/(TPDS) and low energy electron diffraction (LEED) hardware. UHV system contains a double-side polished Pd(111) single crystal with a 1.0 cm diameter and 1 mm thickness. The sample temperature is controlled by a PID unit and DC power supply. Before the experiments, the surface of the palladium crystal is cleaned by several cycles of Ar^+ sputtering and annealing at 1000 K.

The cleanliness of the surface can be sustained under low pressure; therefore UHV system works at ca.10^{-10} Torr. This extremely low pressure can be obtained by baking the chamber. Baking is the heating of the UHV chamber and gives rise to the desorption of the molecules that stick to the walls. The baking temperature is about 90 - 110 °C, but before baking the system, all electronic parts on the UHV chamber should be removed except the cable connected to the ion gauge.

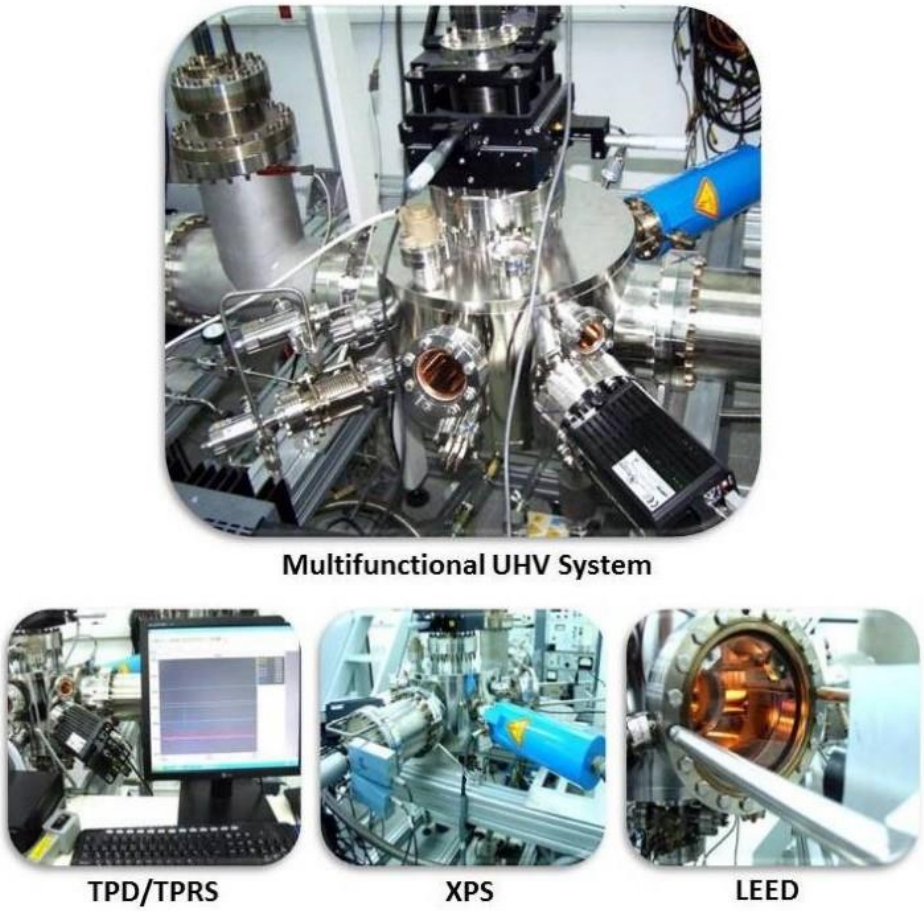

Figure 2.1: Multicomponent UHV system used in the current work.

2.1.1 Gas Manifold

The physical vapor deposition (PVD) (or also called thermal evaporation) technique is used to prepare MnO_x thin films on the Pd(111) surface. The thin film growth compartment includes metal dosers (Figure 2.2). Direct electrical current is passed through the metal doser, which leads to the evaporation of the desired metal on the sample surface under UHV conditions. Tantalum (Ta) legs with high chemical inertness and a high melting point with a diameter of 1 mm are used to hold the metal targets that are evaporated.

2.1.2 Thin Film Doser Compartment

The vapor deposition technique is used to prepare MnO_x thin films on Pd(111) surface. The thin film growth compartment work with direct current, and evaporation of the metals and metal oxides are achieved in the UHV system. Tantalum (Ta) legs with a diameter of 1 mm are used to hold the samples that are evaporated.

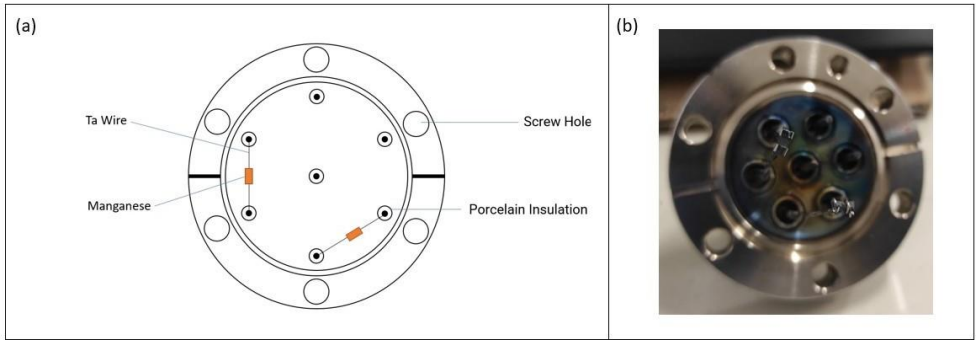

Figure 2.2: (a)Feed through of the metal doser flange, (b) Prepared Mn doser where the Mn piece is sandwiched between Ta plates with a small opening.

To form a MnO_x thin film on Pd(111), 12 A, 1.5 V was used to evaporate the Mn source. Before the evaporation of the Mn, Mn doser was degassed to prevent contamination of the Pd(111) single crystal. Thin films were prepared when the Pd(111) sample was at room temperature and 85 K since the size of the Mn clusters is affected by the temperature of the sample, which is discussed in detail in the forthcoming sections.

2.1.3 Titanium Sublimation Pump (TSP)

A titanium sublimation pump (TSP) removes water from the UHV chamber. It contains titanium filaments, which are heated via direct electrical current to evaporate Ti. Ti coated on the chamber walls reacts with molecules and forms stable compounds, so the pressure in the chamber decreases. However, in time, the adsorption capacity of the Ti thin film produced by the TSP decreases, and

the base pressure of the system starts to increase. Therefore, TSP is used at least once a week.

Regular use of TSP causes Ti filaments to thin over time and eventually become inoperable. Therefore, old titanium filaments should be changed to maintain the effectiveness of the pump. The used TSP pump has two independent filaments, and only one of them can be operated in the system. If the filament is damaged, another filament can be used without venting the system.

2.1.4 Ion Gun

Ion gun (RBD instruments IG2 Model 04-165) is used to clean the surface of the crystal by Ar^+ sputtering (Figure 2.3). Electron gun requires a static Ar pressure of $5x10^{-5}$ Torr. Ar^+ ions are generated by electron impact within the ion source's tungsten filament in the ionization chamber. Then, the Ar^+ beam is focused on the sample with an energy of up to 2 keV. For a given operating pressure and source-to-sample distance, a focusing lens allows for a high ion current density. When the first tungsten filament opens, the dual tungsten filament assembly allows for continued operation.

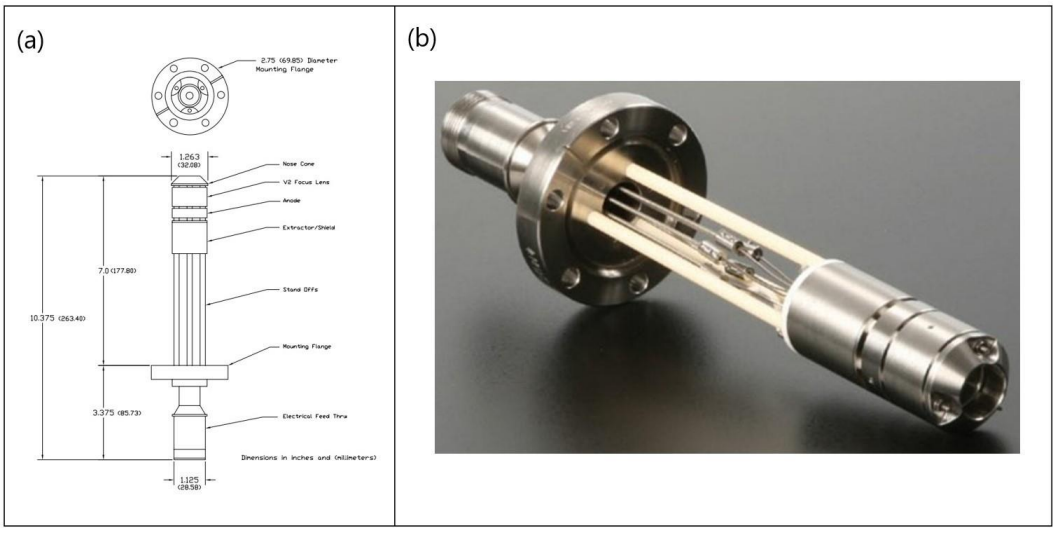

Figure 2.3: (a) Scaled drawing of the ion gun (b) Photograph of the ion gun.

2.1.5 Sample Heating System

The heating system consists of a K-type thermocouple, PID controller, and a DC power supply. PID controller, ORDEL PC 771, adjusts the current, which is applied to the heating wire in the sample to reach the set point. PID controller determines how much and how quickly correction is applied by using three actions [71]. These three actions are P(Proportional), I(Integral), and D(Derivative). The controller produces an output signal to operate the final control element, which is a triac. PID controller uses the P, I, and D actions and multiplies each parameter by the error, E [72]. Error is the difference between the set point and process variable, which can be formulated as 2.1.

$$E = SP - PV \tag{2.1}$$

SP: Set Point
PV: Process Value

Proportional control, P, reduces process variable fluctuation but does not bring the system to the intended set point. P response is faster than other controllers; however, a high P value can cause a deviation from the set point [73]. This deviation is called as offset, which is not a desirable process. The presence of an offset can cause fluctuations at the set point. By adjusting I and D parameters, the offset can become negligible; however, complete offset elimination is impossible.

Integral control, I, another feedback control and can remove deviations from the set point. Integral control takes a role in both negative error and positive error. The main difference between P and I controllers is that I has a much slower in its response time than P controller. The main advantage of the integral controller, it can decrease the offset. However, increasing the I controller in the PID system can cause a destabilization since the fast response of the P term is suppressed by I.

Derivative control, D, is pretty different from P and I controllers. D controller

minimizes the change by considering the process condition. The derivative control, D, acts on the rate of change measured in the process variable [74]. The leading advantage of D controller is to prevent change in the system. Moreover, control can also provide a faster response in the loop, but D is negatively affected by the noisy signal of the P control. However, in general, P control generates a very clean signal, which makes the D control unnecessary.

Tunning a PID controller is not an easy process. Although there is an autotune option in PC 771, trial and error was the main method to make proper adjustments. Current P, I, and D values are 320, 80, and 1.0, respectively.

K-type thermocouple is used to measure the temperature of the sample. Two different alloys (Chromel and Alumel) are used in the K-type thermocouple, and the temperature interval of K type thermocouple is between 70 K and 1500 K. The highest and lowest temperature used during the current experiments were 85 K and 1000 K.

2.2 Surface Sensitive Analytical Techniques

2.2.1 X-Ray Photoelectron Spectroscopy (XPS)

X-Ray photoelectron spectroscopy (XPS) is a useful technique to determine the elemental and oxidation state analysis of the samples. In this technique, electrons of the atoms on the sample are ejected from the sample due to the X-Ray radiation. Ejected electrons from the sample provide information about the oxidation state, and atomic composition [75]. The kinetic energy of the ejected electron from the sample is measured by an energy analyzer. The binding energy of the electron can be measured by using the following formula:

$$E_b = hv - E_k - \phi \qquad (2.2)$$

E_b :Binding energy of core electron
hv :X-ray photon energy

E_k :Kinetic energy of the photoelectron
ϕ :Kork function of the spectrometer (4.5 eV)

The XPS system is equipped with an Al and Mg dual anode source, which can be individually utilized. The dual anode is useful when Auger and XPS peaks appear at the same binding energies. By using the different X-Ray sources (Mg and Al), Auger and XPS peaks can be distinguished. In the current XPS experiments, 8 kV, 25 mAh was applied to produce Mg K_α X-ray radiation [76]. During the X-Ray production, the anode should be cooled; therefore, the current Al-Mg dual anode X-Ray source has a water cooling system.

Hemispherical energy analyzer and double-pass mirror analyzer are used in XPS spectrometers to measure the binding or kinetic energy of the electrons. The current multifunctional UHV system includes a double-pass cylindrical mirror analyzer (DPCMA), Riber EA 150. Two concentric cylindrical electrodes create an electric field with cylindrical symmetry in the DPCMA. The outer cylinder is held at a negative potential while the inner cylinder is at a positive potential. The number of electrons that enter the analyzer is determined by their initial kinetic energy. The voltage difference between the inner and outer cylinders is kept constant throughout the voltage scan, resulting in a constant pass energy resolution (i.e., retarding mode). Changing the electrostatic field in front of the analyzer allows the scanning at different energies. This is achieved by employing spherically shaped grids that decelerate incoming electrons, allowing for increased resolution at higher electron energies [77, 78].

A hemispherical analyzer (HMA) is more commonly used in XPS devices due to its higher resolution than double-pass cylindrical analyzers. It works by deflecting photoelectrons coming from the surface due to a potential difference. Because photoelectrons with higher kinetic energies have a longer flight time than photoelectrons with lower kinetic energies, they will hit a different spot on the detector plane. As a result, HMA uses different trajectories followed by photoelectrons to resolve photoelectron kinetic energies.

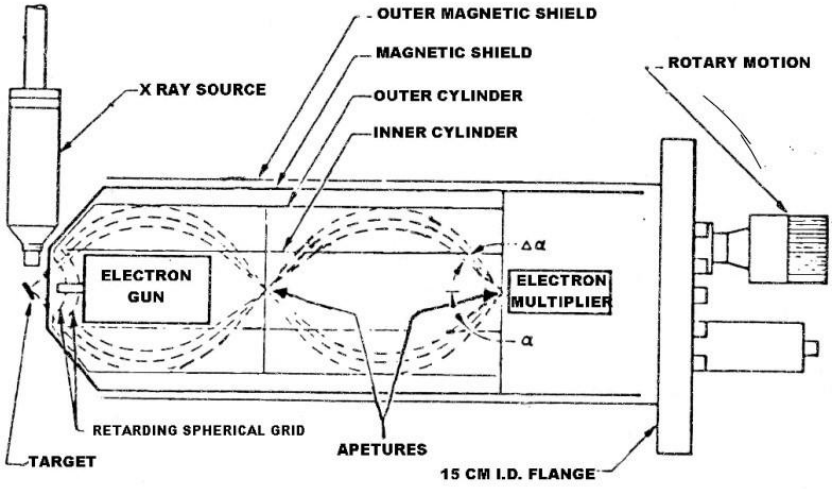

Figure 2.4: Schematic of the double-pass cylindrical mirror analyzer. Adapted from Ref. [6].

A RS-285 connection provides communication between the double-pass mirror analyzer and computer. When the length of the cable becomes more than 5 m, undesired spectral artifacts (such as artificial peaks) in the spectrum are observed in the current experimental setup.

XPS was not used to check the cleanliness of the Pd(111) sample. Due to the low sensitivity of the currently used DPCMA-based XPS system, C1s signal was not observed. XPS was used to determine the thin film growth mechanism of the manganese film on Pd(111) and the concentration of the Mn^{0}, Mn^{2+} and Mn^{3+} on formed catalyst.

2.2.2 Temperature Programmed Desorption (TPD)

Temperature programmed desorption (TPD) is the most sensitive surface technique in the current UHV system. Thermodynamic and kinetic information about the desorption processes of adsorbed atoms/molecules on a substrate is provided via TPD by heating the sample linearly with a constant heating rate of 1 K/s in front of the quadrupole mass spectrometer (QMS, Ametek Dycore Dymaxion

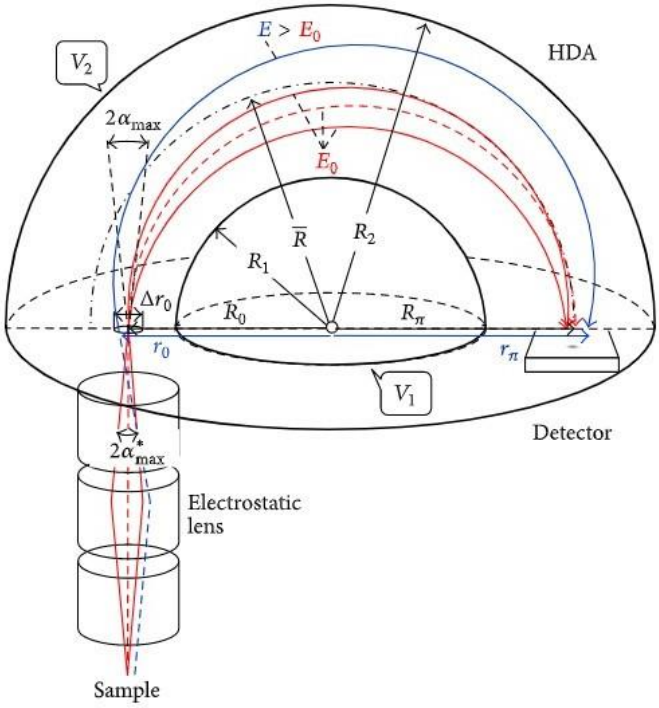

Figure 2.5: Schematic of the hemispherical analyzer. Adapted from Ref. [7].

DM200). An electron impact ionization energy of 70 eV was used in the QMS ionization chamber. When the eight channels were used to make TPD experiments, dwell time was adjusted to 30 ms.

Because the QMS signal is proportional to the rate of desorption if the pumping speed is large enough in TPD/TPRS experiments, the structure of the partial pressure curve as a function of temperature includes information about desorption kinetics [79]. The Polanyi-Wigner equation shows how desorption rate, desorption energy, desorption order, and temperature are related [8].

$$r = -\frac{d\Theta}{dt} = k_{des}\Theta^{n} = \nu(\Theta)\,\Theta^{n}\exp\left[-\frac{E_{des}(\Theta)}{RT}\right] \tag{2.3}$$

$$T = T_0 + \beta t \tag{2.4}$$

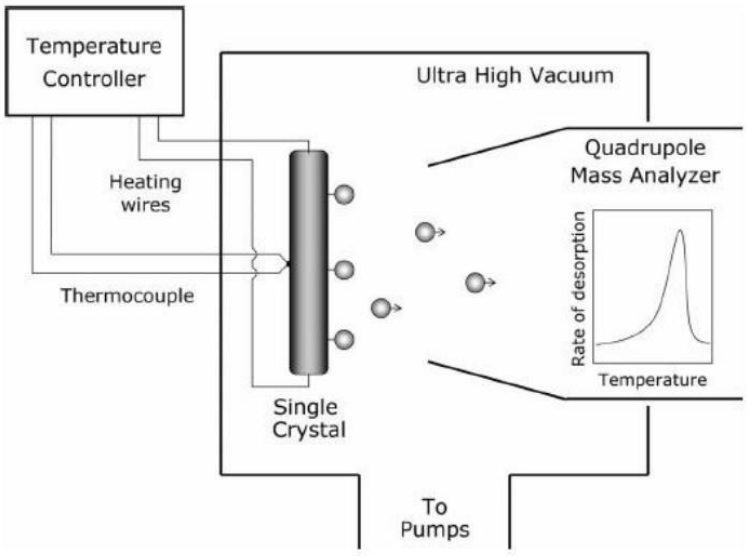

Figure 2.6: TPD experimental setup in the UHV system. Adapted from Ref. [8].

where:

r: rate of desorption

Θ : adsorbate coverage in monolayers t : time

k_{des} : reaction rate constant for the desorption

n : order of the desorption

ν : pre-exponential factor of the desorption

E_{des} : activation energy of the desorption R : gas constant

T_0 : initial temperature of the sample

β : heating rate

The desorption process does not practically occur when the E_{des} is greater than RT. Peak shape is affected by desorption order in TPD. Zeroth (n=0), first (n=1), and second-order (n=2) desorption curves are given in Figure 2.7.

The desorption rate does not depend on the coverage at zero-order desorption, and it generally occurs in multilayers[80]. On the other hand, the desorption rate is proportional to the coverage on first-order (n=1) desorption kinetics.

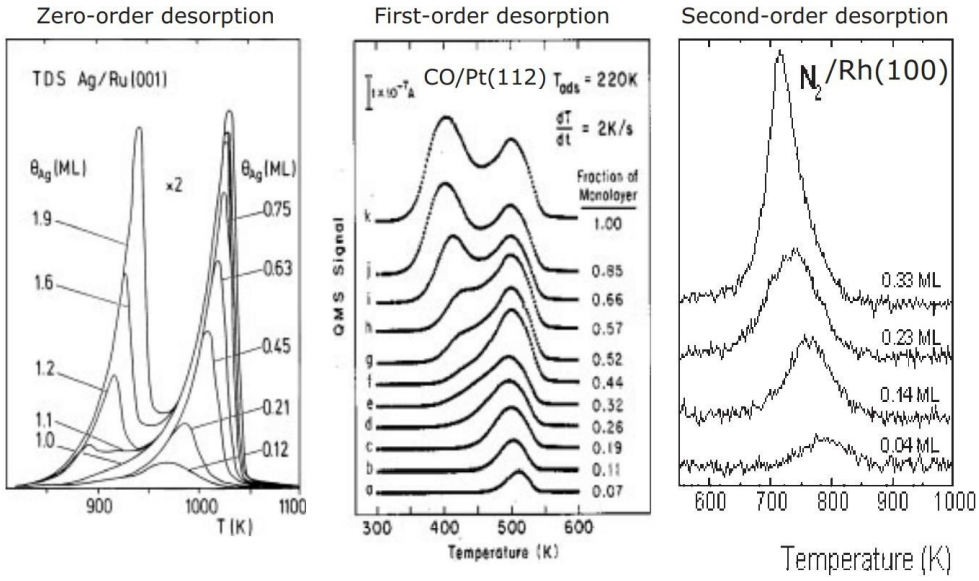

Figure 2.7: TPD spectra for zeroth, first and second order desorption kinetics. Adapted from Ref. [9].

Another characteristic property of the first-order desorption is that different coverages have a unique desorption peak shape. For atomic and non-dissociative reversible adsorption/desorption of molecules, first-order desorption behavior is common. When the surface of the substrate is fully covered with the adsorbate for the adsorbate overlayer following layer-by-layer growth mode, non-dissociative desorption intensities for sub-monolayer coverages converge to a saturation intensity. This saturation point can be used to calculate the relative coverages of the other desorption curves quantitatively [9]. The desorption peak maximum shifts to lower temperatures as a function of adsorbate coverage in second-order desorption kinetics (n=2). Second-order desorption is common in recombinative desorption of atoms/molecules after dissociative adsorption.

Thermodynamic information, such as adsorption and desorption enthalpies, can also be obtained via TPD spectra. Although kinetic parameters depend on the desorption enthalpy, which relies on the adsorbate coverage, thermodynamic information can be derived by making some approximations. For molecules with first-order desorption kinetics, for instance, the adsorbate's desorption enthalpy can be calculated by using the Redhead equation [81]. The pre-exponential factor to the heating rate, ν/β, ratio is between 10^{8} and 10^{13} K^{-1} in the Redhead

equation, and kinetic parameters are assumed to be coverage independent [81]. 10^{8}-10^{13} K^{-1} is commonly used as the pre-exponential factor. The TPD signal of experimental peak maximum is replaced with T_{max} in the Redhead formula, and the desorption energy of adsorbate can be calculated. The redhead equation is given below.

$$E_{des} = RT_{max}\left[\ln\left(\frac{\nu T_{max}}{\beta}\right) - 3.64\right] \quad (2.5)$$

2.2.3 Low Energy Electron Diffraction (LEED)

The surface structure of single crystals and the ordered adsorbate layers can be determined by using low-energy electron diffraction (LEED). However, by using LEED, adsorption sites of the atoms on a single crystal cannot be determined, it gives information only on the overall symmetry [82]. In LEED, a beam of monoenergetic low-energy electrons (50-200 eV) having a small mean free path collides with surface/sample electrons and is scattered elastically in all directions. The mean free path of the electrons depends on their kinetic energy, which in turn dictates the surface sensitivity. The ultimate surface sensitivity in LEED can be obtained using electrons having an energy within 25 -200 eV (Figure 2.8).

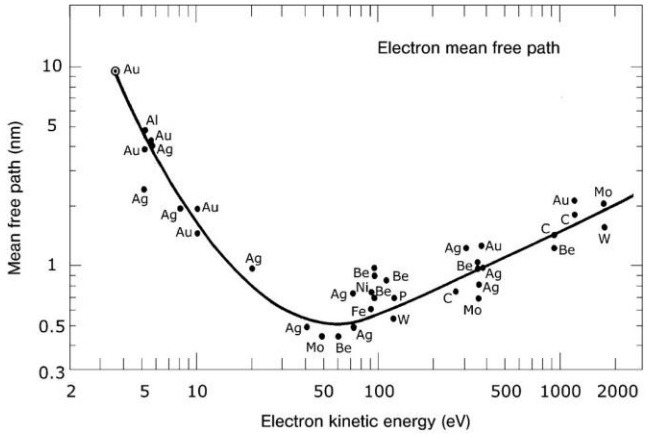

Figure 2.8: Electron inelastic mean free path values of electrons in various metals as a function of electron kinetic energy Ref. [8].

In a LEED setup, the incident electron beam is generated by thermionic

emission under ultra-high vacuum conditions. Accelerated electrons hit the sample surface and are scattered. Scattered electrons are collected by the fluorescence screen that has 2-5 kV positive potential (Figure 2.9).

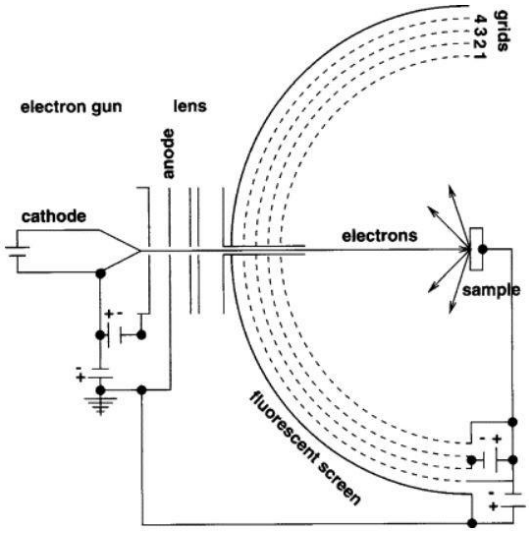

Figure 2.9: LEED setup. Adapted from Ref.[10].

In a LEED experiment, electrons behave like waves, which was explained by the French physicist Louis de Broglie in his 1924 Ph.D. thesis. Louis de Broglie received the Nobel Prize for Physics in 1929 for the explanation of the wave nature of electrons [83]. The relationship between the kinetic energy of the electrons and wavelength is given by:

$$\lambda = \frac{h}{\sqrt{2 m_e E_k}} \tag{2.6}$$

where:
h, J.s, Planck's constant
m_e , kg, Mass of electron
E_k , kinetic energy of the electron
λ, wavelength of the electron

Secondary electrons with lower kinetic energy than the backscattering electrons cannot contribute to the LEED pattern on the fluorescent screen. Elastically scattered electrons that have constructive interference give information

about the crystallinity of the surface and the structure of the well-ordered adsorbent by creating visible patterns on the fluorescent screen. Surface lattice ($n\lambda = d$) can be determined by the 2D-Bragg equation.

$$d = n\lambda = a \sin\alpha \tag{2.7}$$

where:
n is the order of diffraction
λ is the wavelength of the electrons
a is the distance among the atoms on the surface
α is the angle between surface normal and scattered electrons

LEED pattern on the fluorescent screen belongs to reciprocal space and is represented by vector a_j^*, j=1,2. The real space surface unit cell vectors are represented by a_i, i=1,2, and LEED pattern is the Fourier transform of the real space lattice. The scalar product relation connects the reciprocal vectors to the real space unit cell vectors.

$$a_1 \cdot a_1^* = a_2 \cdot a_2^* = 1 \tag{2.8}$$

$$a_1 \cdot a_2^* = a_1^* \cdot a_2 = 0 \tag{2.9}$$

There are two common types of the notation to describe the LEED pattern, matrix notation and Wood's notation [84]. Lattice vectors c_1 and c_2 in overlayer surface structures can be different from the a_1 and a_2 in the substrate. But they can be written as follows using the substrate lattice vectors.

$$c_1 = m_{11}a_1 + m_{12}a_2 \tag{2.10}$$

$$c_2 = m_{21}a_1 + m_{22}a_2 \tag{2.11}$$

These lattice vectors can be expressed by a matrix.

$$\begin{pmatrix} c_1 \\ c_2 \end{pmatrix} = \begin{pmatrix} m_{11} & m_{12} \\ m_{21} & m_{22} \end{pmatrix} \begin{pmatrix} a_1 \\ a_2 \end{pmatrix} \tag{2.12}$$

which can be represented as

$$c = M \cdot a \tag{2.13}$$

Reciprocal lattice vectors can be defined as

$$b^* = M^* \cdot a^* \tag{2.14}$$

where

$$M^* = \begin{pmatrix} m_{11}^* & m_{12}^* \\ m_{21}^* & m_{22}^* \end{pmatrix} \tag{2.15}$$

These matrices can be directly connected using standard matrix algebra, so it gives the following expression.

$$\begin{pmatrix} m_{11} & m_{12} \\ m_{21} & m_{22} \end{pmatrix} = \frac{1}{\det M^*} \begin{pmatrix} m_{22}^* & -m_{21}^* \\ -m_{12}^* & m_{11}^* \end{pmatrix} \tag{2.16}$$

If the required reciprocal lattice vectors can be extracted from the observed diffraction pattern, the connection is sufficient to allow true lattice structure to be deduced from the observed diffraction pattern [85].

Wood's notation is another and more frequently used method to express LEED patterns. Wood's notation can be used when two-unit cells have the same or closely related symmetries. In the Wood's notation two different lattice vectors a_1, a_2 and b_1, b_2 are defined. Overlayer structures can be defined by the lattice vectors. Wood's and matrix notation examples for some selected overlayers are given in Figure 2.10.

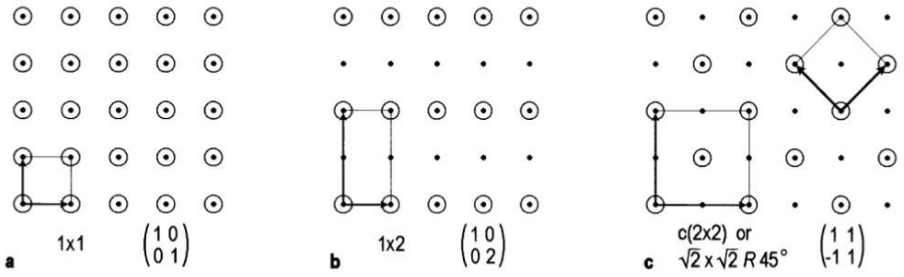

Figure 2.10: Examples for Wood's and matrix notations of selected overlayers. adapted from Ref. [11].

Chapter 3

Results and Discussion

3.1 Cleaning of the Pd(111) Single Crystal

Cleaning of the Pd(111) single crystal was achieved by three different procedures. If the sample contamination is high, which typically occurs after the venting of the UHV system, the sample was exposed to molecular oxygen (O_2 Purity ≥ 99.999 %) at 600 K by using a tube doser. The pressure of the O_2 is adjusted to 2.5×10^{-9} Torr and the temperature of the sample is sustained at 600 K for 20 minutes. Next Ar^+ sputtering was carried out ($P_{Ar} = 5 \times 10^{-5}$ Torr, I_{beam} = 7 μA, 15 min) followed by annealing at 1000 K for 10 min.

If the surface is moderately contaminated second method is used. The second method to clean the sample utilized Ar^+ sputtering and annealing cycles. Such a cleaning cycle begins with Ar^+ sputtering ($P_{Ar} = 5 \times 10^{-5}$ Torr, I_{beam} = 7 μA, 7.5 min) and ends with annealing at 1000 K for 10 min. The last process was called flashing. If the sample waits for a long time (> 2 h) in the chamber at UHV conditions, only flashing is enough to form a clean surface. Flashing is heating the sample until 1000 K at about 2 min so that the quick heating (flashing) readily enables the desorption of the contaminant molecules from the Pd(111) single crystal.

Annealing time for 7.5 minute Ar^+ sputtering determined by performing an O_2 TPD. After the sample is sputtered, Pd(111) surface becomes defective, where annealing heals the surface defect. If the annealing temperature and time are more than enough to heal the defects, molecules like O_2 desorbs without a change in the shape of the TPD peak. Figure 3.1 shows the O_2 desorption after the same Ar sputtering with different annealing time.

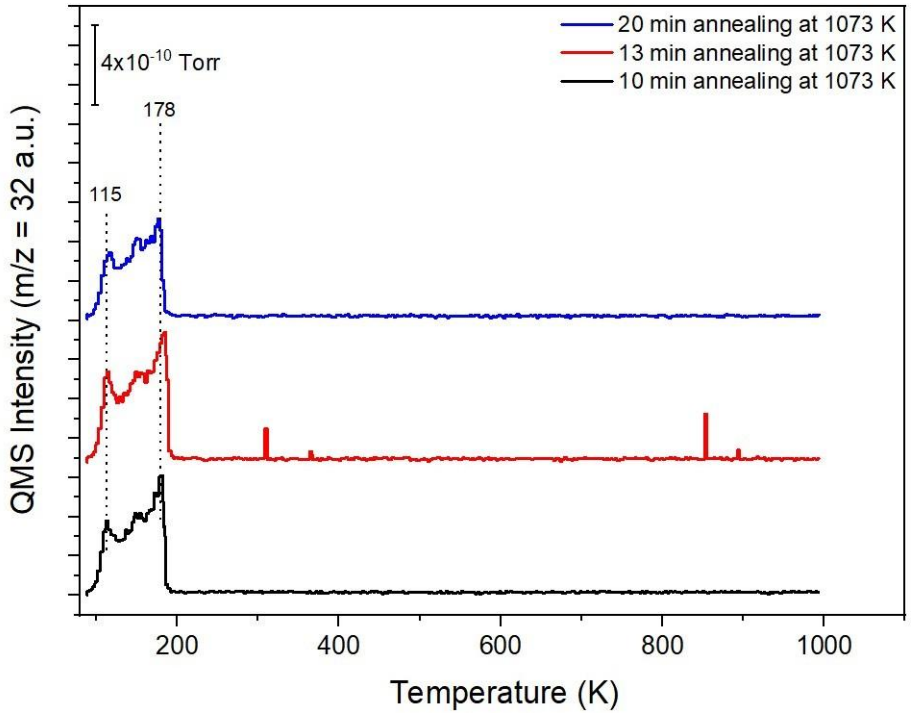

Figure 3.1: O_2 TPD after various time of annealing at 1000 K. O_2 was dosed at 85 K and exposure is 0.3 L (1 L = 10^{-6} Torr · s).

CO is one of the main contaminats on the Pd(111) single crystal. CO is adsorbed on the surface of the crystal strongly, and cleaning of the sample can be achieved by several cycles of Ar^+ sputtering. The cleanliness of the sample was checked by blank CO TPD and LEED. XPS could not be used to check cleanliness since the detection limit of the currently utilized XPS system is not high enough to observe minuscule amounts of surface carbon and oxygen species.

After the Ar^+ sputtering cycles, (blank) CO TPD (Figure 3.2) data were obtained to monitor the cleanliness of the Pd(111) single crystal.

The cleanliness of the sample is also observed by LEED. Clean Pd(111)

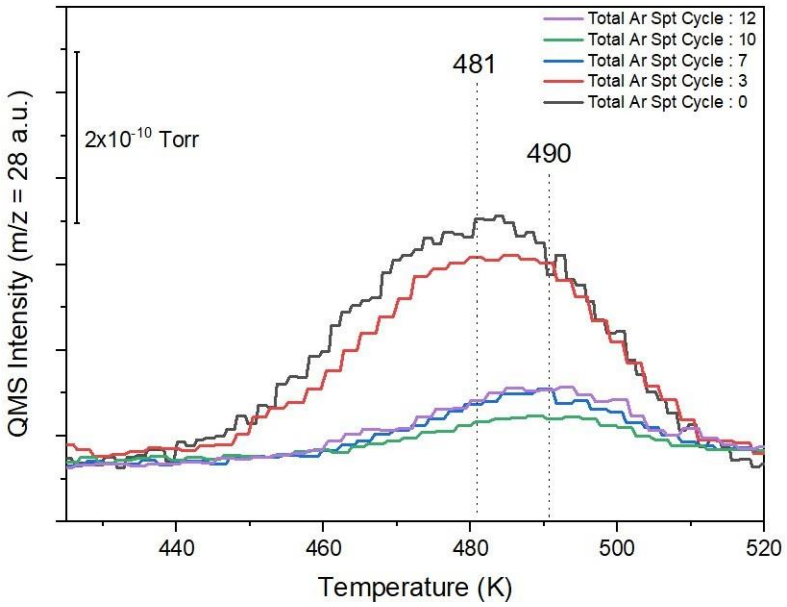

Figure 3.2: Blank CO TPD shows that after 12 cycles of Ar sputtering Pd(111) sample is clean.

LEED hexagonal pattern on the fluorescence screen can be seen in Figure 3.3. The electron beam energy is 70 eV and voltage on the screen is 5 kV.

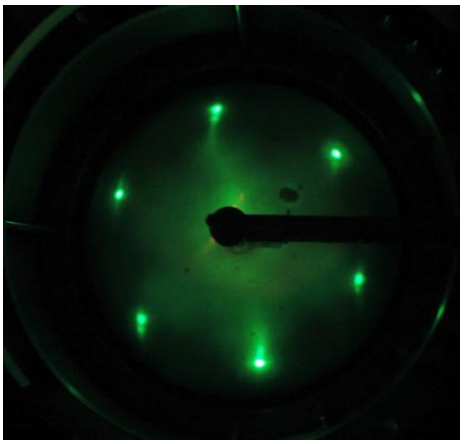

Figure 3.3: LEED pattern of clean Pd(111) single crystal.

3.2 Adsorbate Gas Exposure

Pressure in the UHV chamber is measured by a Bayard-Alpert type ionization gauge. Ionization gauge can measure the pressure down to $2x10^{-11}$ Torr [86]. In the ionization gauge, electrons are produced by ThO_2 coated iridium filaments and are accelerated with an electric field. Some of the accelerated electrons collide with the gas molecules and positively charged ions are generated. A negatively charged collector wire collects the positively charged ions, and a cationic current is measured and converted to pressure.

The unit of exposure is Langmuir (L) (1 L = 10^{-6} Torr.s) [9]. During the experiments, a dedicated tube (pin-hole) doser is used to dose $^{13}CO_2$, CO_2, D_2, and H_2 gases to the Pd(111) sample. In Figure 3.4, a tube doser and other parts of the multifunctional UHV system can be seen.

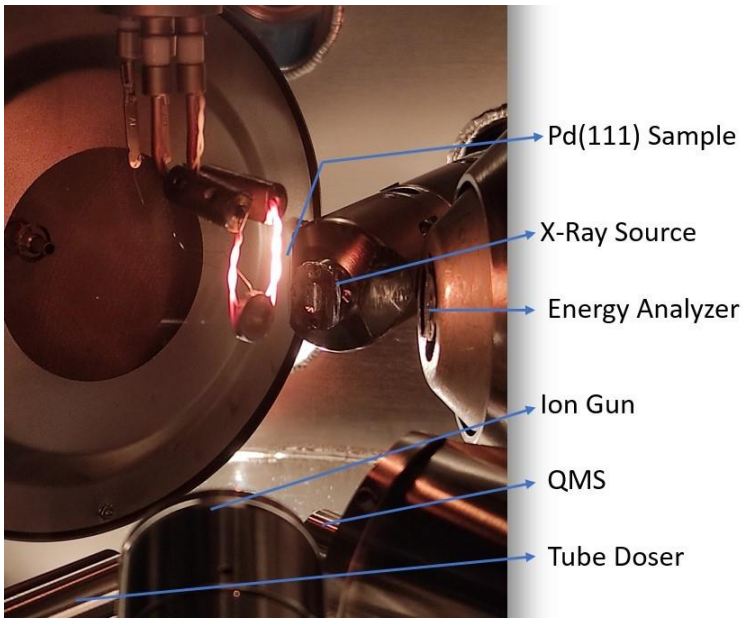

Figure 3.4: Tube doser, QMS, ion gun, energy analyzer, X-Ray source and Pd(111) sample in the UHV chamber.

3.3 CO_2 Adsorption on the Pd(111) Single Crystal

CO_2 physisorbs on the Pd(111) surface while hydrogen is dissociatively adsorbed on the Pd(111) surface. Relative interaction strengths of CO_2 and H_2 with the Pd(111) surface are demonstrated by TPD (Figure 3.5).

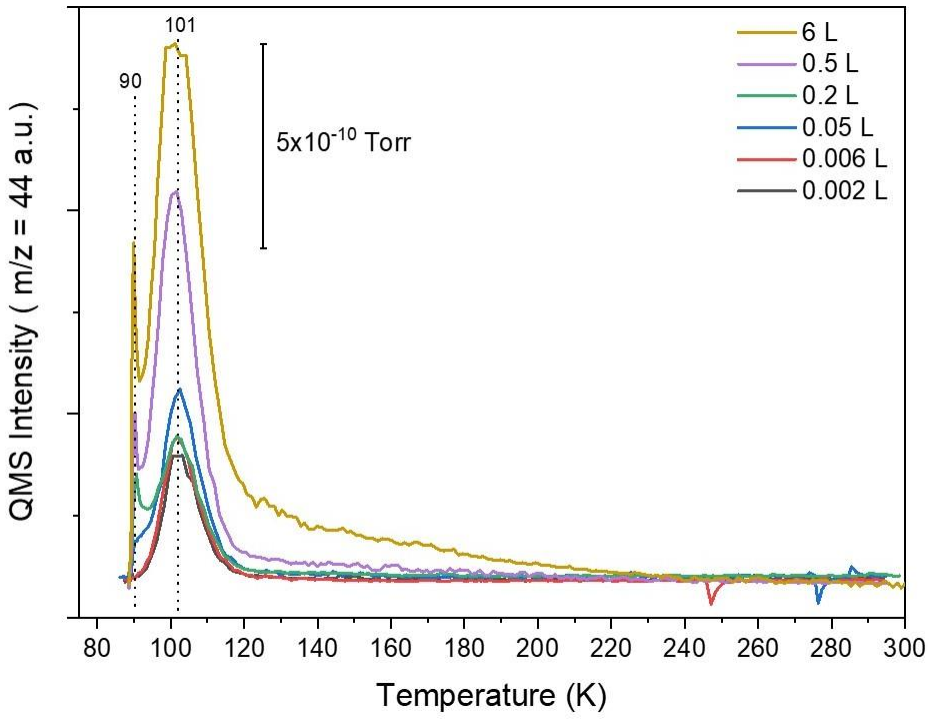

Figure 3.5: CO_2 TPD on clean Pd(111) single crystal. One channel (m/z=45) is used to take a high resolution data while dwell time is 120 ms.

The peak appearing at 90 K can be attributed to multilayer CO_2 [87]. It is expected to reveal zeroth order desorption from the surface [9]. The multilayer CO_2 desorption peak cannot be fully detected in the current experimental setup, as this peak appears at a temperature lower than the minimum attainable temperature in the current system. Physisorption of CO_2, i.e., the second peak, appears at 101 K, revealing a first-order desorption behavior corresponding to the submonolayer coverages CO_2 which are directly interacting with the

Pd(111) surface. By using the Redhead equation, CO_2 desorption energy in the first monolayer is estimated to be 20.5 kJ/mol.

Isotopically labelled CO_2 ,i.e., $^{13}CO_2$, was used in order to differentiate CO_2 existing in the UHV chamber Although the two molecules' molecular masses are different, adsorption and desorption kinetics are similar, as can be seen in Figure 3.6.

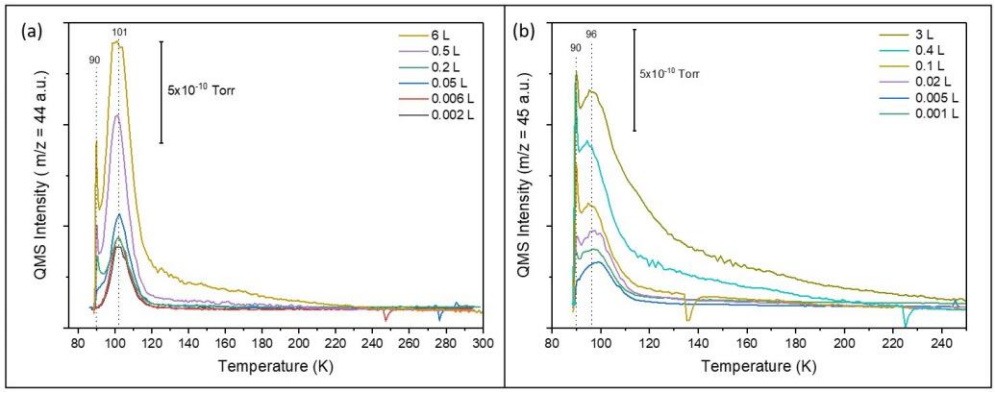

Figure 3.6: TPD spectra for (a) CO_2, (b) $^{13}CO_2$ on Pd(111).

In figure 3.6, although multilayer coverage desorption temperature of CO_2 and $^{13}CO_2$ are the same, submonolayer desorption temperatures are slightly different. (For CO_2 : 101 K and for $^{13}CO_2$: 96 K) There is no activation for the physisorbed CO_2 and $^{13}CO_2$ molecules since both of them have linear geometry on the Pd(111) surface.

3.3.1 H_2 on Pd(111)

On the other hand, H_2 has a stronger binding energy than CO_2 on Pd(111) which is evident by the higher desorption maxima of hydrogen as compared to that of CO_2. Second-order desorption kinetics of H_2 is illustrated in Figure 3.7.

Relatively high recombinative desorption temperature (> 300 K) of the adsorbed hydrogen atoms is consistent with the fact that hydrogen adsorbs strongly

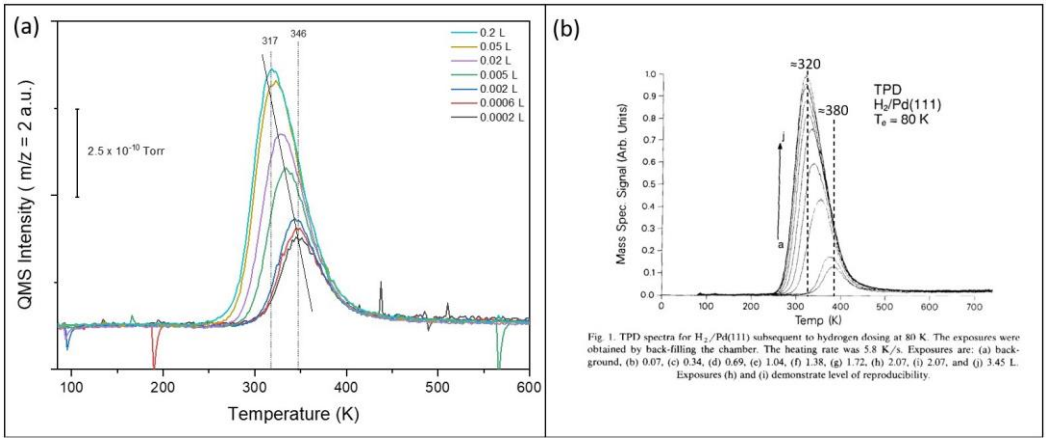

Figure 3.7: (a) TPD spectra of H_2 on clean Pd(111) surface, (b) H_2 TPD on clean Pd(111) surface from the literature. Adapted from Ref. [12].

on the Pd(111) single crystal. Desorption maxima shift to lower temperatures in the H_2 TPD on Pd(111) with increasing hydrogen coverages due to the second-order dissociative kinetics because increasing atomic hydrogen coverage on the Pd(111) surface results in increasing repulsive interactions among adsorbates. As shown in Figure 3.7, saturation hydrogen coverage is achieved around 0.05 L hydrogen exposure when the sample at 85 K in front of the tube doser.

Precise H_2 coverage on the Pd(111) single crystal is difficult to obtain since hydrogen pressure in the chamber is relatively high because of the small size of the molecule. Therefore, D_2 was also used to make further TPD experiments.

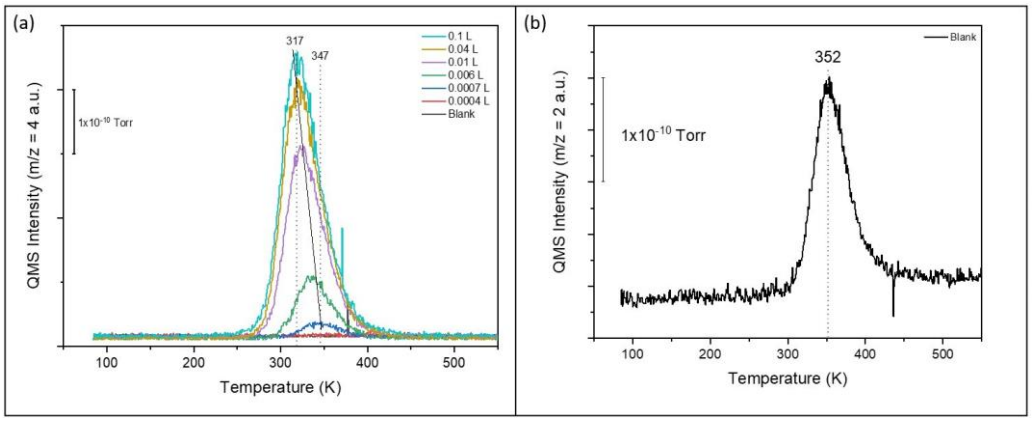

Figure 3.8: (a) TPD spectra of D_2 on clean Pd(111) single crystal, (b) H_2 TPD of the blank Pd(111) single crystal.

Figure 3.8 shows the TPD spectra of D_2 and H_2 on clean Pd(111) surface. Due to the base pressure of the H_2 into the chamber, considerable peak of the H_2 on the blank TPD was observed. On the other hand, blank TPD of the sample did not yield any D_2. Moreover, desorption temperature of the H_2 and D_2 are very similar. When D_2 is dosed on to the sample, HD formation (m/z = 4) was also observed in the TPD spectra. HD formation can be seen in Figure 3.9, which is also illustrated in Figure 3.10.

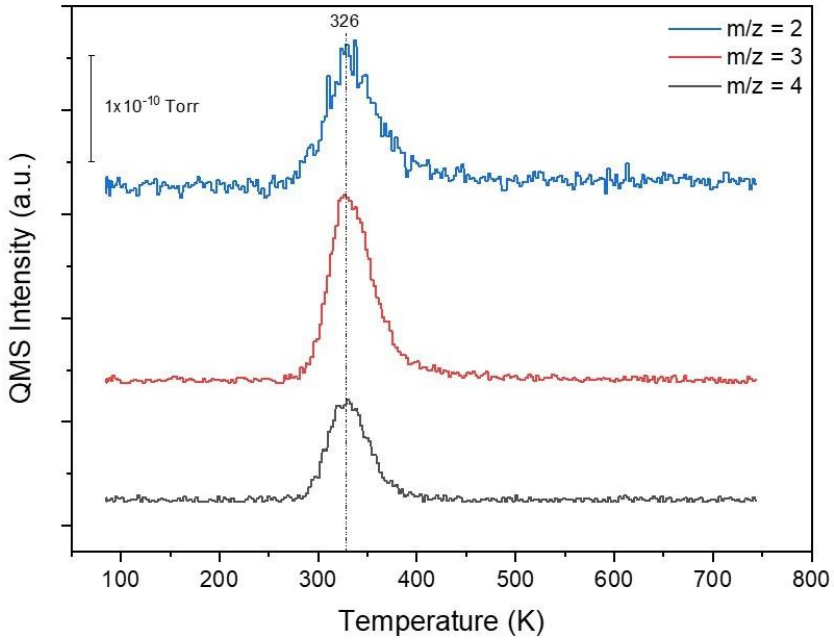

Figure 3.9: TPD spectra of HD formation. D_2 exposure 0.02 L at 85 K and H_2 exposure is 0 L. m/z = 2 H_2, m/z = 3 HD and m/z = 4 D_2.

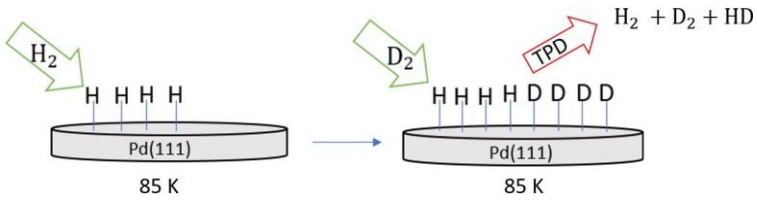

Figure 3.10: Dissociative H_2, and D_2 adsorption and their recombinative desorption on Pd(111) surface.

3.4 Growth of MnO_x Thin Film on Pd(111)

There are three common thin film growth mechanisms, which are Frank-van der Merve(layer by layer), Stranski-Krastanov (layer + island), and Volmer-Webwer (island) [88, 89, 90] (Figure 3.11). The thin film growth mechanism can be determined by using XPS. To do this, the adsorbate/adsorbent XPS peak intensities can be plotted as a function of the adsorbate exposure time.

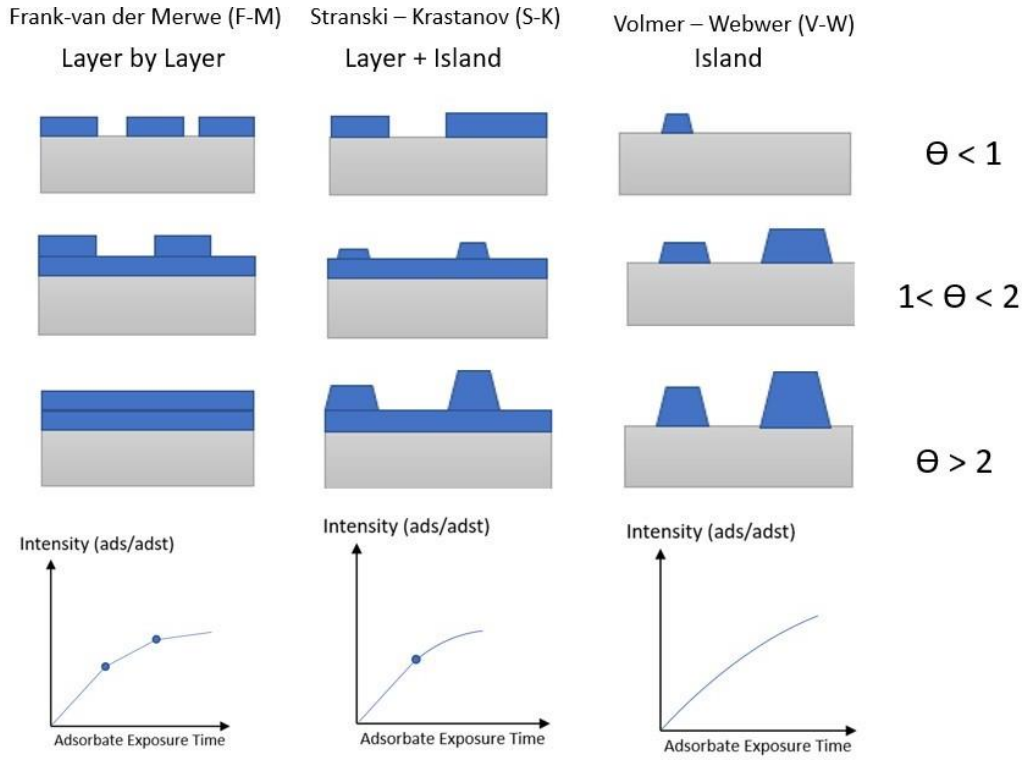

Figure 3.11: Thin film growth mechanisms and the corresponding XPS peak adsorbate/adsorbent intensity ratio change with respect to the adsorbate coverage.

To understand the thin film growth mechanism of the manganese overlayer on Pd(111), adsorbate/adsorbent XPS intensity ratios were measured for several Mn coverages. When the Pd(111) single crystal was at 85 K, the thin film growth mechanism was investigated. Mn dosing was done by the thermal evaporation method by using 15 A.

Manganese thin film growth mechanism on Pd(111) single crystal surface was investigated by using the $2p_{3/2}$ and $Pd_{5/2}$ XPS intensities at different coverages (Figure 3.12).

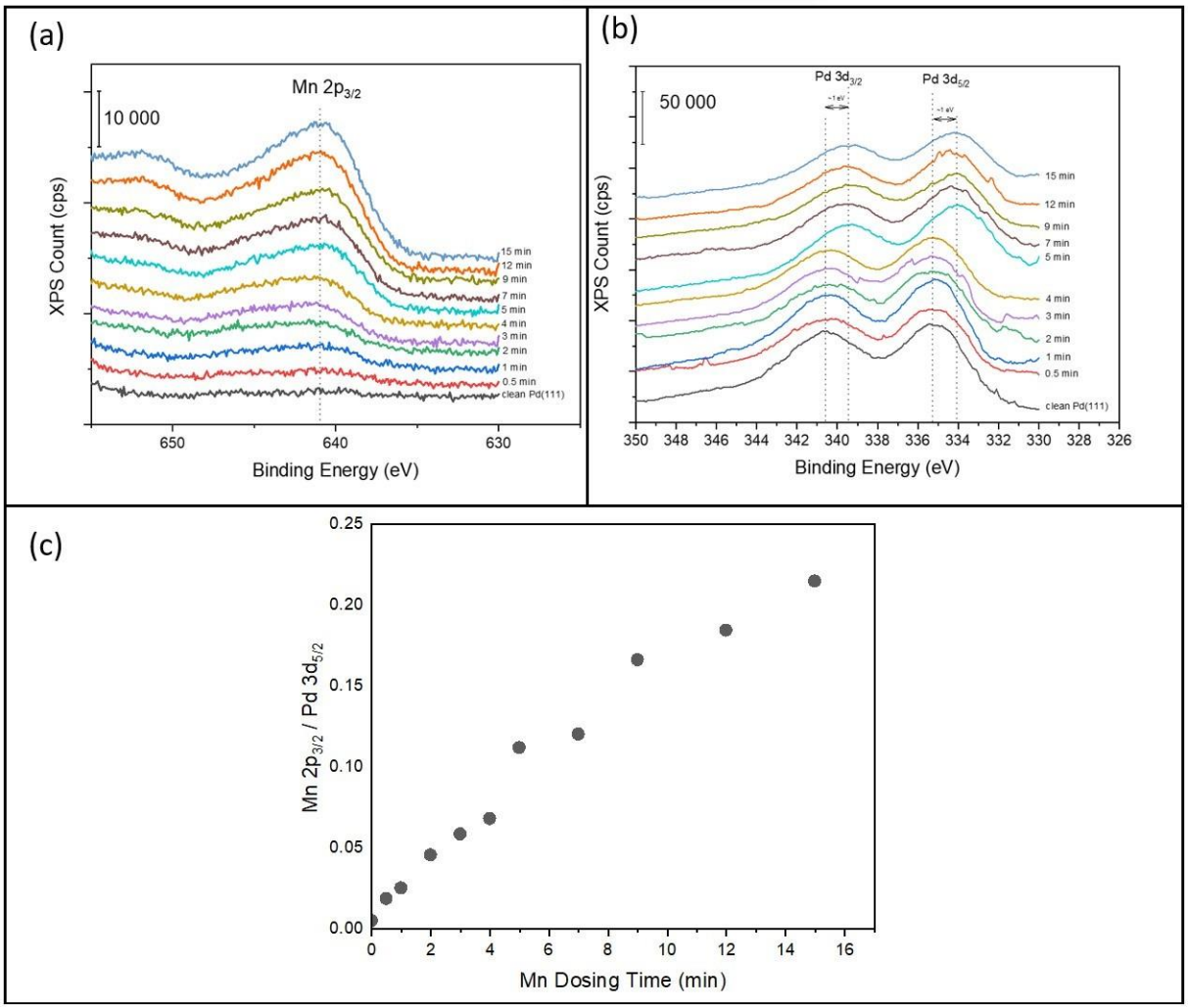

Figure 3.12: (a) Mn $2p_{3/2}$ XPS for various Mn coverages, (b) Pd $3d_{3/2}$ and Pd $3d_{5/2}$ for various Mn coverages (c) XPS intensity ratio of Mn $2p_{3/2}$/Pd $3d_{5/2}$ with respect to manganese evaporation(dosing) time.

Mn $2p_{5/2}$ peak was below the detection limit of the spectrometer. At the highest Mn coverage, Mn $2p_{5/2}$ peak was slightly observable at around 651 eV (Figure 3.12.a). Secondly, in Figure 3.12.b, approximately 1 eV shift was observed on the Pd 3d XPS with increasing the Mn coverage on Pd(111) surface. This can be attributed to the electron transfer from the manganese film to the

palladium.

$Mn\,2p_{3/2}/Pd\,3d_{5/2}$ intensity ratio at different Mn evaporation time was also plotted but a clear break point was not observed (Figure 3.12.c) After the 1 min Mn dosing, it seems there is a break point, which means that the thin film growth mechanism of Mn on Pd(111) surface is between the Layer + Island and Island growth mechanism. Therefore, approximately 1 min Mn evaporation, causes approximately 1 ML thin film formation. 1.5 ML of the MnO_x is formed by dosing 90 seconds of manganese at 15 A.

Cluster size of the MnO_x affects the catalytic properties of the MnO_x/Pd(111) catalyst. The average cluster size of the MnO_x films on the Pd(111) single crystal depends on the temperature ratio of the adsorbate/adsorbent, which can be explained by Sanders classification [91]. In current work, MnO_x/Pd(111) catalyst was prepared using two different conditions. In the first case, manganese was dosed when the Pd(111) single crystal was at room temperature. In the second case, manganese oxide thin film on Pd(111) when the sample temperature was at 85 K.

According to Sanders classification, T and T_m represent the temperature of the adsorbate and adsorbent respectively [91]. When T/T_m is between 0.3 and 0.5, relatively big clusters are obtained, which is the case for the manganese thin film creation at room temperature. When T/T_m becomes smaller than 0.1, smaller cluster formation is possible on the adsorbent.

3.4.1 Preparation of MnO_x Thin Film on Pd(111) Substrate at Room Temperature

When the Pd(111) sample is at room temperature, Mn source was heated with 15 A direct current to evaporate Mn on the Pd(111) single crystal. Manganese oxide thin film with a 1.5 monolayer coverage on Pd(111) single crystal at room temperature could convert the CO_2 to CO and also adsorb the hydrogen (Figure 3.13).

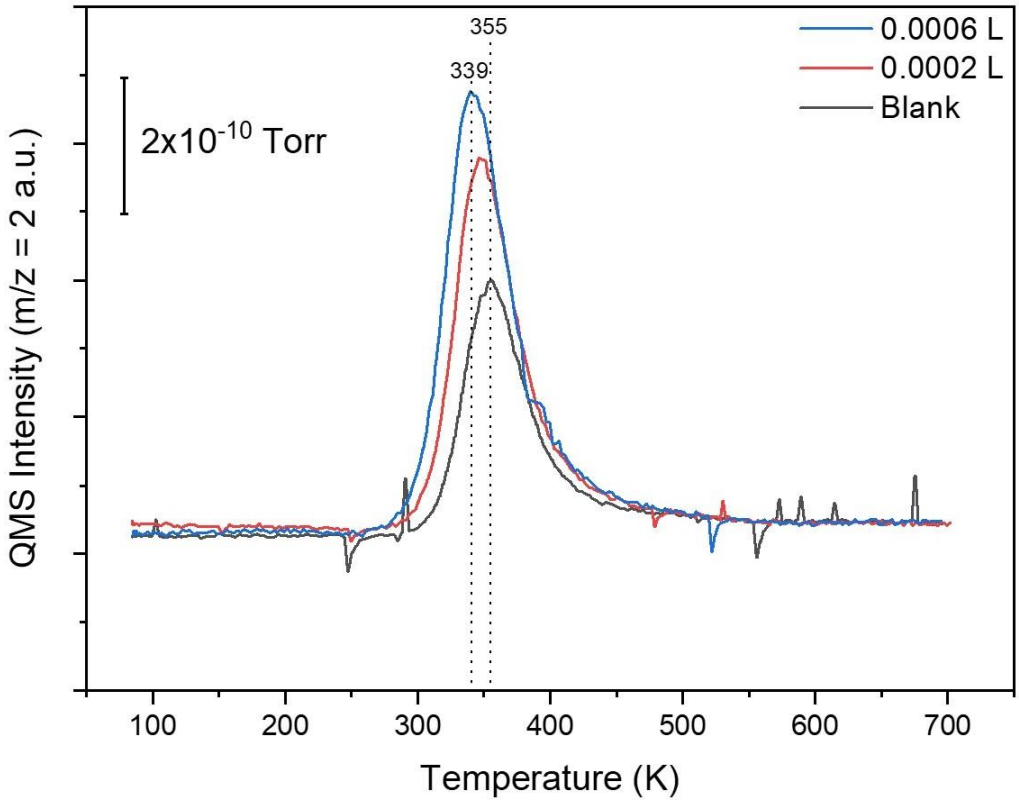

Figure 3.13: Hydrogen TPD on MnO_x/Pd(111) surface. Manganese evaporation was carried out when the sample at room temperature. θ_{MnO_x} = 1.5 ML.

Hydrogen adsorption on the Pd(111) surface that is covered with 1.5 ML MnO_x shows that the palladium sites are available. After the oxidation of the MnO_x /Pd(111) catalyst, 12 L of CO_2 was dosed on the model catalyst surface at 85 K and the CO production was observed in TPD spectra.

TPD spectra in Figure 3.14 shows that the intensity ratio of the carbon monoxide (m/z = 28) to carbon dioxide (m/z = 44). CO_2 fragmentation in the mass spectrometer also generates m/z = 28, and m/z = 44, signals with an intensity ratio 1 and 10, respectively. Therefore, the peak appearing at 486 K shows that CO is the product, since only 10% CO formation of the m/z =28 signal originates from the CO_2 fragmentation in QMS.

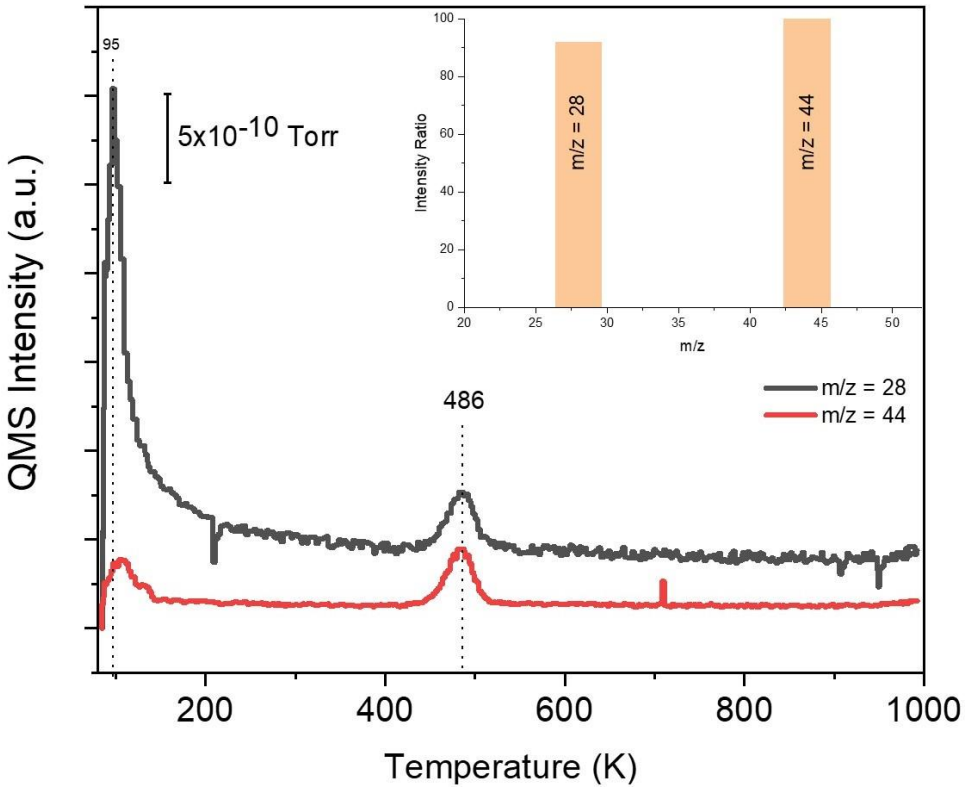

Figure 3.14: CO production on oxidized (with 12 L O_2) 1.5 ML MnO_x /Pd(111) catalyst formed at room temperature after 3 L CO_2 dosage at 85 K. Intensity ratio of the CO and CO_2 at 486 K is shown on the bar graph.

Formed MnO_x 1.5 ML thin film on Pd(111) single crystal was investigated under XPS to determine the oxidation state of the manganese clusters. However, this catalyst could not produce CO as much as the oxidized catalyst formed at room temperature. Figure 3.15a shows the CO production of the oxidation free catalyst that contain 1.5 ML MnO_x on Pd(111) single crystal.

In Figure 3.15b shows XPS spectrum of the 1.5 ML MnO_x film on Pd(111) formed at room temperature (298 K). Unfortunately oxidized MnO_x thin films, in figure 3.14, could not be investigated under XPS due to low resolution.

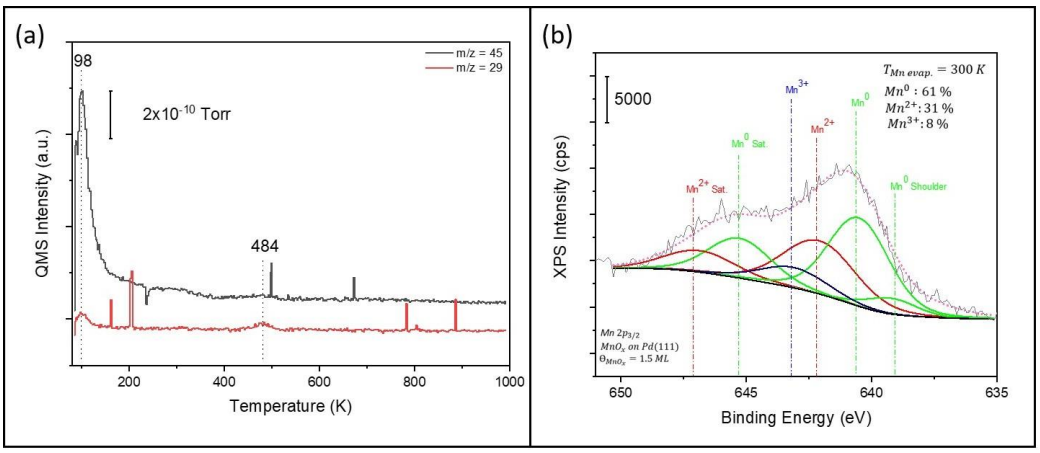

Figure 3.15: (a) m/z = 29, ^{13}CO and m/z = 45, $^{13}CO_2$ TPD spectra of the 1.5 ML MnO_x/Pd(111) catalyst prepared at 300 K without oxidation which was obtained upon 0.4 L $^{13}CO_2$. (b) Mn 2 $p_{3/2}$ XPS spectrum of the corresponding 1.5 ML MnO_x /Pd(111) catalyst prepared at room temperature.

3.4.2 Preparation of MnO_x Thin Film on Pd(111) Sub-starate at 85 K

MnO_x thin film was also prepared when the Pd(111) single crystal was at 85 K. During this film formation, T/T_m was observed to be smaller than 0.1. This particular MnO_x thin film with a moderate coverage at 85 K, could activate the CO_2. Therefore, size of the MnO_x particles was shown to have an important role in activating the CO_2 molecule. TPD data supports the CO_2 activation is observed in Figure 3.16.

In Figure 3.16, it is apparent that at submonolayer Mn coverages CO_2 activation is possible. When the Mn coverages increase, a decrease in the intensity of the α_2 shows the desorption of the $^{13}CO_2$ between the manganese thin film and Pd sides. However, this desorption α_2 is caused by the physisorbed $^{13}CO_2$ molecules in the interfacial sites. On the other hand, α_1 desorption is caused by the physisorbed $^{13}CO_2$ molecules on the palladium sides, which is consistent with the CO_2 TPD data of the clean Pd(111) surface (Figure 3.16). Due to the temperature difference between the α_1 and α_2 peaks, it can be argued that desorption of the $^{13}CO_2$ from the palladium manganese oxide interfacial site has stronger binding energy with CO_2 than pure palladium side.

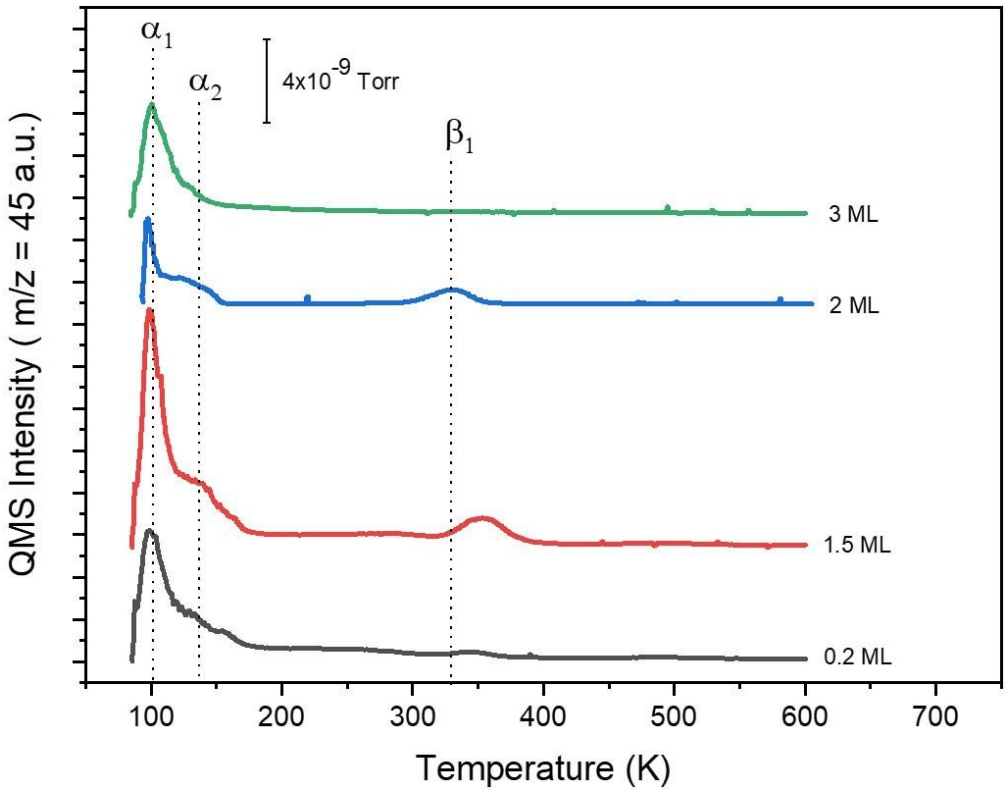

Figure 3.16: $^{13}CO_2$ TPD data obtained for MnO_x films grown on Pd(111) with different coverages at 85 K. 3 L $^{13}CO_2$ and D_2 were dosed by using dedicated tube dosers at 85 K before the TPD measurements. Desorption maxima: α_1 : 100 K, α_2 : 138 K and β_1 : 338 K.

β_1 peak visible at 338 K corresponds to $CO_2^{\delta-}$ and/or CO_3^{2-} species on interfacial sites. This can also be activated form of the CO_2 molecule with a bent structure. This desorption process is observed at moderate manganese oxide coverages and becomes maximum when the MnO_x thin film coverage is approximately 1.5 ML. At higher coverage of MnO_x ($\theta \geq 3$), β_1 peak disappears. This is due to the low number of interfacial sites. When the coverage is approximately 0.2 ML, β_1 peak intensity is barely observable. MnO_x /Pd(111) surface that is prepared at 85 K with 1.5 ML of MnO_x was investigated by changing the $^{13}CO_2$ exposure in Figure 3.17.

β_1 peak shifts to the higher temperature when the manganese oxide coverage becomes 1.5 ML. We do not have a clear explanation for this situation. When

the manganese oxide coverage becomes 1.5 ML, carbonate-like species bond more strongly that the Pd(111) surface covered with 2 ML manganese oxide. However, 1.5 ML manganese oxide coverage formed at 85 K gave the consistent data for the β_1 desorption with different labelled CO_2 exposures, which can be seen on Figure 3.17.

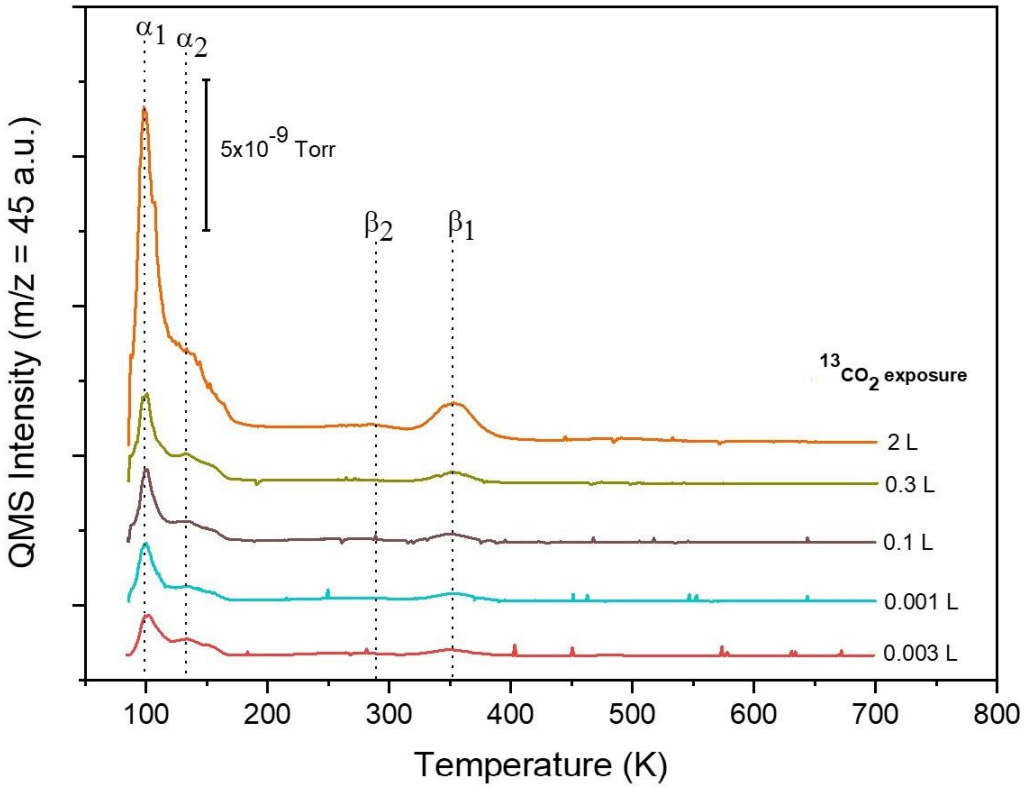

Figure 3.17: Different exposures of $^{13}CO_2$ on MnO_x/Pd(111) system with having a manganese oxide coverage of 1.5 ML formed at liquid nitrogen temperature.

Peak areas of the labeled TPD signals given in Figure 3.17 as a function of carbon dioxide coverage is given on Figure 3.18. Increasing the $^{13}CO_2$ exposure at 85 K leads to higher peak areas for α_1, α_2, and β_2. However, peak area of the β_1 stays almost constant with increasing the $^{13}CO_2$ coverage on the MnO_x/Pd(111) surface.

In Figure 3.17, TPD spectra of Pd(111) single crystal covered with 1.5 ML MnO_x after various $^{13}CO_2$ exposure at 85 K can be seen. β_1 peak reveals a consistent desorption temperature with that of Figure 3.16, i.e., 352 K. When exposure of the labelled CO_2 is increased another peak, i.e., β_2, desorption occurs. β_2 peak is probably associated with the desorption of weakly bonded $CO_2^{\delta-}$ and/or CO_3^{2-} species on manganese oxide palladium interfacial sites. Moreover, according to the TPD spectra in Figure 3.18, physisorbed $^{13}CO_2$ is more than the activated (chemisorbed, carbonate-like molecules). In addition, carbonate like species (β_1 and β_2) increase when the $^{13}CO_2$ coverage is higher. After 2 L exposure of the MnO_x /Pd(111) surface with $^{13}CO_2$, saturation occurs.

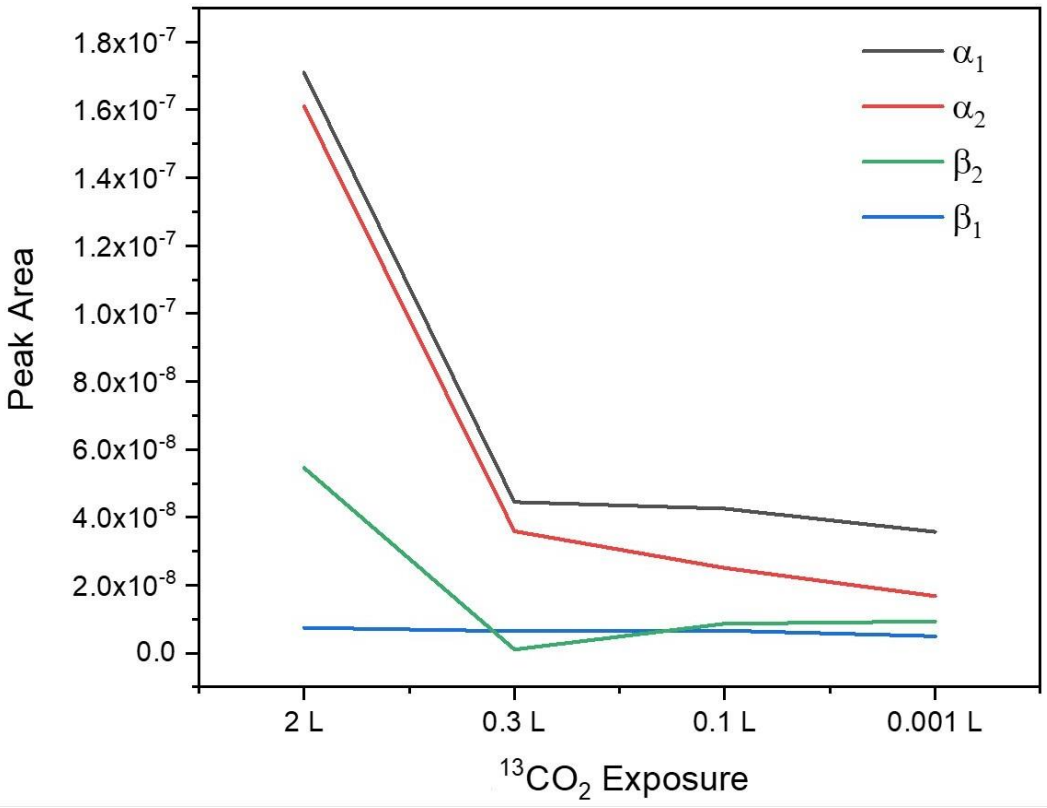

Figure 3.18: m/z = 45 peak areas of α_1, α_2, β_1 and beta$_2$ TPD signals in Figure 3.17. α_1 and α_2 peaks are the physisorbed $^{13}CO_2$ molecules. β_1 and β_2 are carbonate like species on the Pd-MnO_x interfacial sites.

Carbonate-like species on the manganese palladium interfacial sites could be formed with spillover reactions. Although we do not have a clear evidence

for this mechanism, spillover reaction mechanism can explain the occurrence of carbonate like species on the MnO_x/Pd(111) catalyst. During hydrogen spillover hydrogen migration occurs from metal to metal-oxide side. In MnO_x /Pd(111) model planer catalyst a similar event probably occurs since oxygen molecules on the manganese oxide layer can react with the CO_2 molecules on the palladium sides. In this reaction, weakly physisorbed molecules on the palladium side can spill over the manganese oxide sites, and on the interfacial sites of Pd and MnO_x carbonate formation occurs.

After each TPD experiment Ar^+ sputtering was done to remove the agglomerated MnO_x film on Pd(111). Due to the agglomeration of MnO_x on Pd(111) at high temperatures (>600 K), the number of interfacial sites decreases, therefore, β_1 and β_2 peaks disappear, which means that CO_2 activation does not take place.

3.5 Possible Intermediates

1.5 ML MnO_x thin film formed at the liquid nitrogen temperature is the most promising catalyst. Therefore, possible intermediate formations for the methanol are investigated by TPD. 1.5 ML MnO_x thin film on Pd(111) was prepared at 85 K and 15 L $^{13}CO_2$ and 1 L D_2 were dosed at liquid nitrogen temperature before the TPD experiment. Overall reaction for the methanol formation from the CO_2 is given in Eqn 3.1:

$$3\,H_2 + CO_2 \longrightarrow CH_3OH + H_2O \qquad (3.1)$$

Different channels in the quadrupole mass spectrum were recorded spontaneously, such as m/z = 31 (formyl $D^{13}CO$), 35 (methanol), 20 (D_2O, 4 (D_2), 3 (DH) and 45 ($^{13}CO_2$). Moreover, two more reactions could also be observed in the carbon dioxide reduction. Methane (CH_4) and reverse water gas shift reaction (RWGS) can occur on the catalyst surface as shown Eqn. (3.2 and 3.3) below:

$$CO_2 + 4\,H_2 \longrightarrow CH_4 + 2\,H_2O \qquad (3.2)$$

$$CO_2 + H_2 \rightleftharpoons CO + H_2O \qquad (3.3)$$

Due to these to reactions, m/z = 21 (methane) and m/z = 29 (CO) were investigated. In Figure 3.19 TPD spectrum for the possible intermediates and the products can be seen.

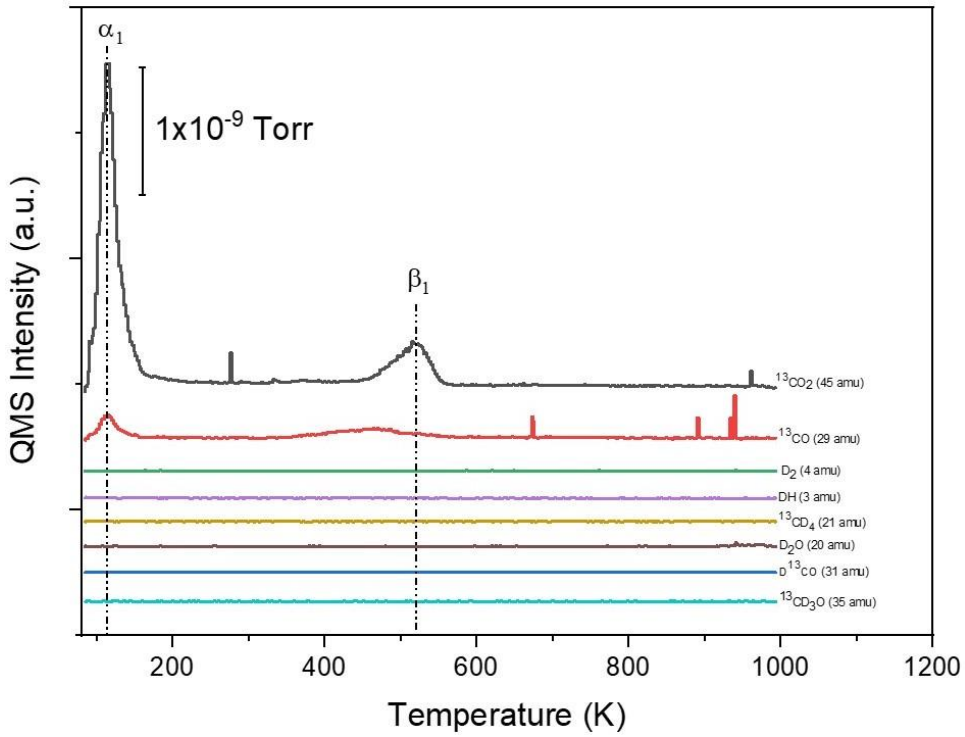

Figure 3.19: TPD profiles for possible detectable products due to CO_2 hydrogenation on MnO_x /Pd(111) surface formed at liquid nitrogen temperature.

However, except for CO and $^{13}CO_2$ peaks, any other intermediate or product does not exist in the spectra. Peaks coming at 114 K and 510 K are not related to the RWGS reaction since there is no sign of water desorption from the

surface in the TPD spectrum. α_1 peak for $^{13}CO_2$ and CO comes from the carbon dioxide fragmentation in the mass spectrometer. Due to the 1:10 intensity ratio of the CO and CO_2, α_1 peak is related to the physisorbed $^{13}CO_2$. The high-temperature peak of the carbon monoxide comes from the chemisorption of the carbon monoxide due to the re-adsorption of the carbon monoxide fragmented of the labeled carbon dioxide in the mass spectrometer.

On the other hand, a $^{13}CO_2$ peak at a higher temperature appears in the TPD. $^{13}CO_2$ peak is observed for the similar surface at around 340 K in 3.16. This shows that the stronger chemisorption occurred between the adsorbate and adsorbent. The absence of the D_2 and DH peaks suggest that the deuterium was consumed due to the formation of other species. One of the possible products is bicarbonate ($D^{13}CO_3^-$). However, a more certain confirmation of the molecules on the surface is impossible due to the lack of IRAS data for bicarbonate on Mn oxides in the literature.

3.6 XPS Analyses of Manganese Oxide Thin Films Grown on Pd(111)

1.5 ML manganese oxide thin films grown on Pd(111) at room and liquid nitrogen temperature are investigated. Due to the experimental limitations, oxidized manganese thin films that are formed at room temperature could not be investigated due to the artifacts in the spectrum.

Manganese thin films on the Pd(111) surface have more than one oxidation state. Mn 2 p XPS signal yields at least two peaks in XPS due to spin-orbit splitting. Splitting occurs due to different values of quantity j, total angular momentum quantum number, i.e., $j = |l \pm s|$, where " l " is the angular momentum quantum number, and s is the spin angular momentum number. On the other hand, spin quantum number can be either +1/2 or -1/2. If there are more than one allowed value of j, spin-orbit splitting is observed in the XP spectrum of the sample. The intensity of the spin-orbit split peaks is related to the degeneracy

(g = 2j+1) of the photo electrons' electronic states. Accordingly, Mn 2 $p_{3/2}$ has two times higher intensity than that of Mn 2 $p_{1/2}$. However, 2 $p_{1/2}$ is below the detection limit of the currently used XP spectrometer. Therefore, only 2 $p_{3/2}$ peak was analyzed in the current work.

3.6.1 XPS of 1.5 ML MnO_x Thin Films Grown on Pd(111) at Room Temperature

1.5 ML manganese oxide thin films grown on Pd(111) surface at room temperature was investigated by using the Mg anode of XPS source. To take the XPS spectrum, 8 kV and 25 mA were applied to the tungsten filament. The sweep of the XPS spectrum is 15 and dwell time (ms) is 1000. Taken XPS, was fitted by using the CasaXPS program. In Figure 3.20 shows the relevant Mn 2 $p_{3/2}$ XP spectrum.

According to Figure 3.20, total concentration of the manganese oxide is less than the metallic manganese. In oxidized manganese, Mn^{3+} concentration is about 8 %, while Mn^{2+} concentration is about 31 %. At approximately 1 ML of the manganese thin films on the various metal surfaces, (such as Pd, Ag, Cu, Ni), Mn 2 $p_{3/2}$ XP binding energy (B.E) for Mn^0 species reveals a higher B.E. than that of pure methalic manganese species [92]. Pure manganese metal reveals a Mn 2 $p_{3/2}$ XP signal at 638.8 eV, which does not coincide with that of the Mn thin film on Pd(111). Hence, the Mn 2 $p_{3/2}$ XP peak located at 640.6 eV is attributed to the metallic manganese peak. Mn^0 has also a strong shake-up satellite and it has approximately 5 eV higher binding energy than that of the main Mn 2 $p_{3/2}$ XP signal of Mn^0. Moreover, Mn^0 shows an additional shoulder peak. Mn^0 shoulder peak are observed on Pd-Mn systems due to the inequivalence of the Mn atoms on the Pd surface [92]. Therefore, three different Mn^0 peaks exhibit in Figure 3.20.

Mn^{2+} exhibits two Mn 2 $p_{3/2}$ peaks located at 642.4 eV and 643.6 eV. Peak

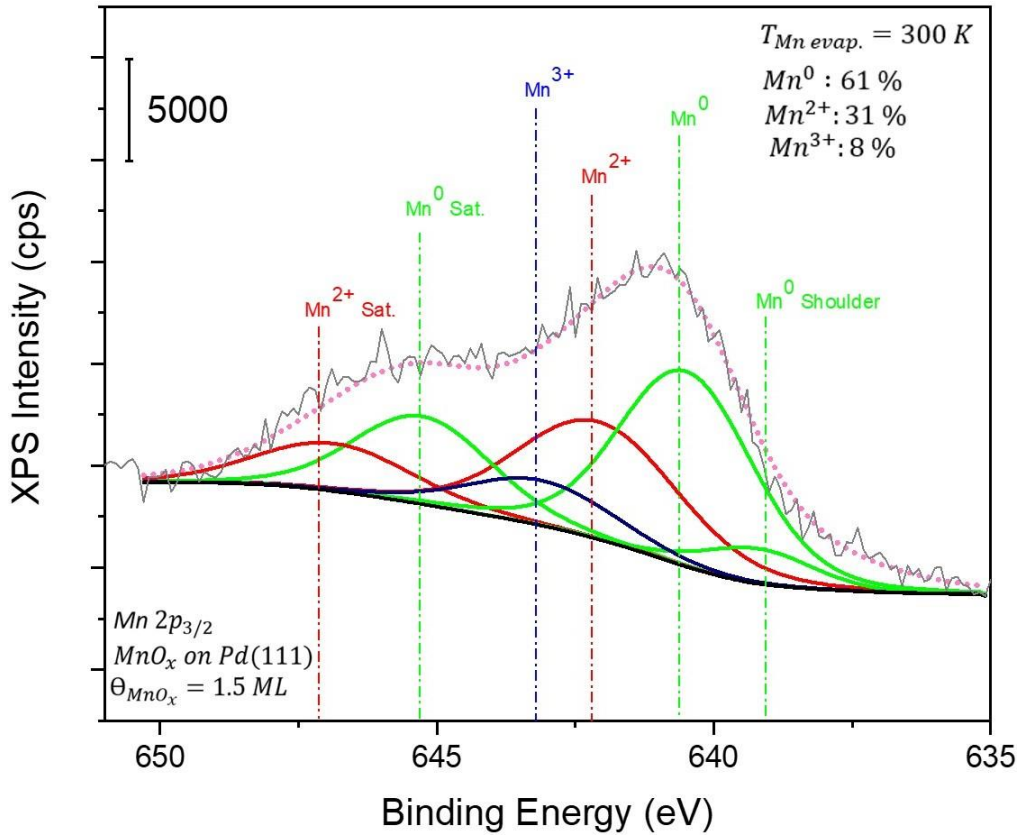

Figure 3.20: XPS of 1.5 ML MnO_x on Pd(111) formed at room temperature.

appearing at 643.6 eV is the shake-up peak of Mn^{2+} which is separated by approximately 6 eV with respected to Mn^{2+} peak [93]. Finally the peak located at 643.3 eV is attributed to the Mn^{3+} [94].

Obtained manganese thin films at room temperature are oxidized by using the molecular oxygen, O_2 by exposing with 2000 L at T = 85 K. At the end of the oxidation process, approximately 56 % Mn^0 concentration was detected but improvement in the CO_2 activation was not observed.

3.6.2 XPS of 1.5 ML MnO_x Thin Film Grown on Pd(111) at 85 K

XPS of 1.5 ML MnO_x thin film formed at 85 K was also analyzed in detail. According to Figure 3.21, oxidized manganese concentration on Pd(111) surface prepared at liquid nitrogen temperature is more than the manganese oxide thin film formed at room temperature at the 1.5 ML coverage. Mn^0 concentration decreases from 61 % to the 51 %. However, Mn^{2+} concentration stays nearly constant, it increases only by 2 %. On the other hand, Mn^{3+} concentration doubles (i.e., an increase from 16 % to 32 %).

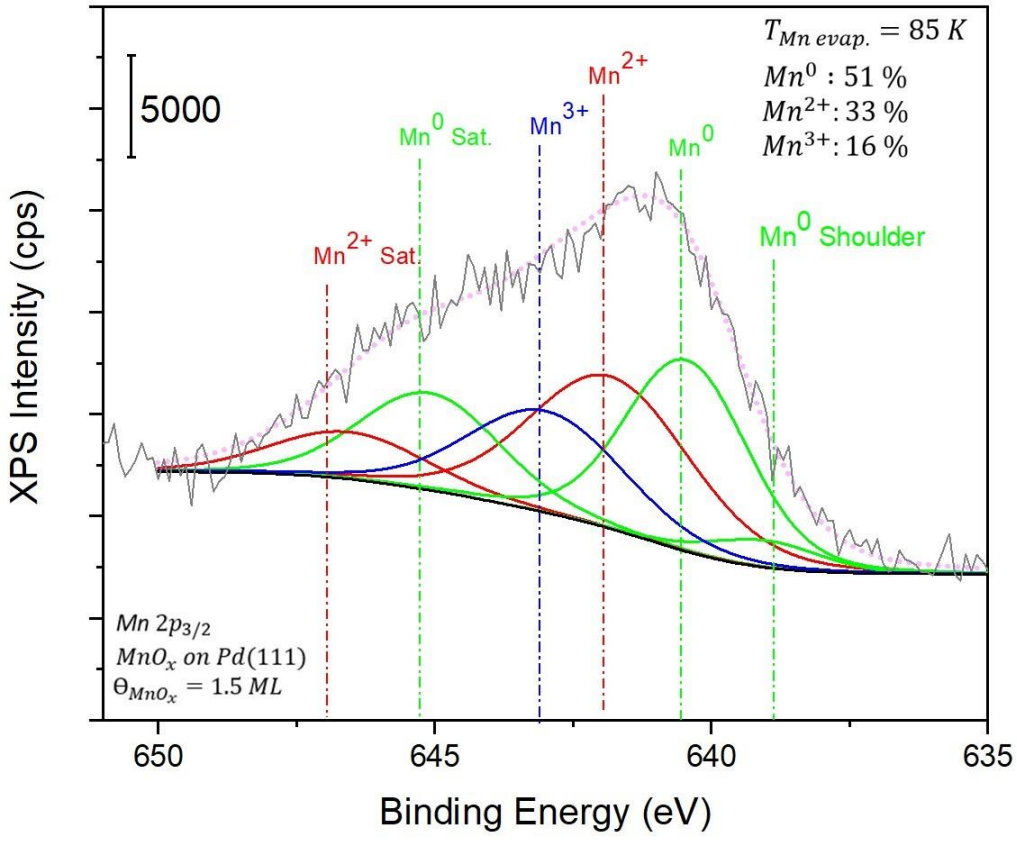

Figure 3.21: XPS of 1.5 ML MnO_x on Pd(111) surface formed at 85 K.

Chapter 4

Conclusion

In conclusion, our findings show that the reactivity of the metal oxide interface can be adjusted by changing the structure of the oxide component to generate the active sites required for CO_2 activation. We investigated the adsorption and activation of CO_2 on a heterogeneous bi-component model catalyst made up of small MnO_x clusters supported on a Pd(111) surface using temperature programmed desorption and x-ray photoelectron spectroscopy techniques. CO_2 activation is significantly improved when the size of MnO_x nanoclusters are reduced by lowering the catalyst preparation temperature to 85 K. It most likely occurs through the formation of carbonate and/or carboxylate-like intermediates, with the interfacial sites, which involve both MnO_x and adjacent Pd atoms, playing a key role. The observed maximum CO_2 activation at less than a monolayer MnO_x coverage is well correlated with the interfacial character of the active sites. High coverages of the MnO_x cause to decrease in the number of interfacial sides; consequently, CO_2 activation does not occur on the surface.

Bibliography

[1] Nakamura, Shinichiro, et al. "A basic quantum chemical review on the activation of CO2." *Advances in CO2 Capture, Sequestration, and Conversion*. American Chemical Society, 2015. 123-134.

[2] Yang, Yong, et al. "Mechanistic studies of methanol synthesis over Cu from CO/CO2/H2/H2O mixtures: The source of C in methanol and the role of water." *Journal of catalysis* 298 (2013): 10-17.

[3] Cui, Chaonan, et al. "A DFT study of CO2 electrochemical reduction on Pb (211) and Sn (112)." *Science China Chemistry* 58.4 (2015): 607-613.

[4] Perşembe, Elif. *Trimetalic Heterogeneous Catalyst for Dehydrogenation of Formic Acid with Enhanced Co Tolerance*. Diss. Bilkent Universitesi (Turkey), 2017.

[5] Ochirkhuyag, Altantuya, et al. "One-pot mechanochemical ball milling synthesis of the MnO x nanostructures as efficient catalysts for CO 2 hydrogenation reactions." *Physical Chemistry Chemical Physics* 22.25 (2020): 13999-14012.

[6] Palmberg, P. W. "A combined ESCA and Auger spectrometer." *Journal of Vacuum Science and Technology* 12.1 (1975): 379-384.

[7] Sise, Omer, and Theo JM Zouros. "Position, energy, and transit time distributions in a hemispherical deflector analyzer with position sensitive detector." *Journal of Spectroscopy* 2015 (2015).

[8] Niemantsverdriet, Johannes W. *Spectroscopy in catalysis: an introduction*. John Wiley & Sons, 2007.

[9] Chorkendorff, Ib, and Johannes W. Niemantsverdriet. *Concepts of modern catalysis and kinetics*. John Wiley & Sons, 2017.

[10] Speller, S., W. Heiland, and M. Schleberger. "1. Surface characterization: Composition, structure and topography." *Experimental Methods in the Physical Sciences*. Vol. 38. Academic Press, 2001. 1-109.

[11] Oura, Kenjiro, et al. *Surface science: an introduction*. Springer Science & Business Media, 2013.

[12] Gdowski, G. E., T. E. Felter, and R. H. Stulen. "Effect of surface temperature on the sorption of hydrogen by Pd (111)." *Surface Science* 181.3 (1987): L147-L155.

[13] Fischer, Michael, Mathew Werber, and Peter V. Schwartz. "Batteries: Higher energy density than gasoline?." *Energy policy* 37, no. 7 (2009): 2639-2641.

[14] Edwards, Peter P., Vladimir L. Kuznetsov, William IF David, and Nigel P. Brandon. "Hydrogen and fuel cells: towards a sustainable energy future." *Energy policy* 36, no. 12 (2008): 4356-4362.

[15] Fang, Zhen, ed. *Liquid, Gaseous and Solid Biofuels: Conversion Techniques*. BoD–Books on Demand, 2013.

[16] Ud, et al. "Recent developments on heterogeneous catalytic CO2 reduction to methanol." *Journal of CO2 Utilization* 34 (2019): 20-33.

[17] Jia, Yufei, et al. "Cu-based bimetallic electrocatalysts for CO2 reduction." *Advanced Powder Materials* 1.1 (2022): 100012.

[18] Singh, Surya, et al. "Ag-Co bimetallic catalyst for electrochemical reduction of CO2 to value added products." *Journal of CO2 Utilization* 18 (2017): 139-146.

[19] Gholinejad, Mohammad, et al. "Applications of bimetallic PdCu catalysts." *Catalysis Science & Technology* 11.8 (2021): 2652-2702.

[20] Zhong, Jiawei, et al. "State of the art and perspectives in heterogeneous catalysis of CO 2 hydrogenation to methanol." *Chemical Society Reviews* 49.5 (2020): 1385-1413.

[21] Jiang, Xiao, et al. "Recent advances in carbon dioxide hydrogenation to methanol via heterogeneous catalysis." *Chemical Reviews* 120.15 (2020): 7984-8034.

[22] Jiang, Feng, et al. "Hydrogenation of CO 2 into hydrocarbons: enhanced catalytic activity over Fe-based Fischer–Tropsch catalysts." *Catalysis Science & Technology* 8.16 (2018): 4097-4107.

[23] Zhang, Minhua, et al. "A DFT study of methanol synthesis from CO2 hydrogenation on the Pd (111) surface." *Catalysis letters* 148.9 (2018): 2935-2944.

[24] Du, Xian-Long, et al. "Research progress on the indirect hydrogenation of carbon dioxide to methanol." *ChemSusChem* 9.4 (2016): 322-332.

[25] Jiang, Xiao, et al. "Bimetallic Pd–Cu catalysts for selective CO2 hydrogenation to methanol." *Applied Catalysis B: Environmental* 170 (2015): 173-185.

[26] Nie, Xiaowa, et al. "Mechanistic understanding of alloy effect and water promotion for Pd-Cu bimetallic catalysts in CO2 hydrogenation to methanol." *ACS Catalysis* 8.6 (2018): 4873-4892.

[27] Peng, Ting, et al. "Photo-driven selective CO 2 reduction by H 2 O into ethanol over Pd/Mn–TiO 2: suitable synergistic effect between Pd and Mn sites." *Catalysis Science & Technology* 11.6 (2021): 2261-2272.

[28] Gibson, Dorothy H. "Carbon dioxide coordination chemistry: metal complexes and surface-bound species. What relationships?." *Coordination chemistry reviews* 185 (1999): 335-355.

[29] Etim, Ubong J., Chenchen Zhang, and Ziyi Zhong. "Impacts of the catalyst structures on CO2 activation on catalyst surfaces." *Nanomaterials* 11.12 (2021): 3265.

[30] Sehested, Jens. "Industrial and scientific directions of methanol catalyst development." *Journal of Catalysis* 371 (2019): 368-375.

[31] Luc, Wesley, et al. "Ag–Sn bimetallic catalyst with a core–shell structure for CO2 reduction." *Journal of the American chemical society* 139.5 (2017): 1885-1893.

[32] Yoo, Chul Jong, et al. "Compositional and geometrical effects of bimetallic Cu–Sn catalysts on selective electrochemical CO2 reduction to CO." *ACS Applied Energy Materials* 3.5 (2020): 4466-4473.

[33] Ma, Ming, et al. "Electrochemical reduction of CO2 on compositionally variant Au-Pt bimetallic thin films." *Nano Energy* 42 (2017): 51-57.

[34] Subramani, Velu, and Santosh K. Gangwal. "A review of recent literature to search for an efficient catalytic process for the conversion of syngas to ethanol." *Energy & fuels* 22.2 (2008): 814-839.

[35] Sofianos, Alkeos C., and Mike S. Scurrell. "Conversion of synthesis gas to dimethyl ether over bifunctional catalytic systems." *Industrial & engineering chemistry research* 30.11 (1991): 2372-2378.

[36] Dean, "Lange's handbook of chemistry," 1999

[37] Wang, Haipeng, et al. "Enhanced photocatalytic CO2 reduction to methane over WO3· 0.33 H2O via Mo doping." *Applied Catalysis B: Environmental* 243 (2019): 771-779.

[38] Dang, Shanshan, et al. "Rationally designed indium oxide catalysts for CO2 hydrogenation to methanol with high activity and selectivity." *Science advances* 6.25 (2020): eaaz2060.

[39] Nam, Dae-Hyun, et al. "Molecular enhancement of heterogeneous CO2 reduction." *Nature materials* 19.3 (2020): 266-276.

[40] Varela, Ana Sofia, et al. "Controlling the selectivity of CO2 electroreduction on copper: The effect of the electrolyte concentration and the importance of the local pH." *Catalysis Today* 260 (2016): 8-13.

[41] Smykowski, Daniel, Bartłomiej Szyja, and Jerzy Szczygieł. "DFT modeling of CO2 adsorption on Cu, Zn, Ni, Pd/DOH zeolite." *Journal of Molecular Graphics and Modelling* 41 (2013): 89-96.

[42] Ye, Jingyun, et al. "Methanol synthesis from CO2 hydrogenation over a Pd4/In2O3 model catalyst: A combined DFT and kinetic study." *Journal of catalysis* 317 (2014): 44-53.

[43] Lou, Yang, et al. "CeO2 supported Pd dimers boosting CO2 hydrogenation to ethanol." *Applied Catalysis B: Environmental* 291 (2021): 120122.

[44] He, Zhenhong, et al. "Synthesis of liquid fuel via direct hydrogenation of CO2." *Proceedings of the National Academy of Sciences* 116.26 (2019): 12654-12659.

[45] Li, Weisong, et al. "MnO x-Promoted, Coking-Resistant Nickel-Based Catalysts for Microwave-Initiated CO2 Utilization." *Industrial & Engineering Chemistry Research* 59.15 (2020): 6914-6923.

[46] Simmons, Gary W., et al. "Oxygen adsorption on palladium (100) surface: Phase transformations and surface reconstruction." *The Journal of Physical Chemistry* 95.11 (1991): 4522-4528.

[47] Strømsheim, Marie Døvre, et al. "CO-Induced Surface Reconstruction of the Co (11–20) Surface—A Combined Theoretical and Experimental Investigation." *The Journal of Physical Chemistry C* 124.52 (2020): 28488-28499.

[48] d'Agostino, A. T., and P. N. Ross Jr. "LEED/electrochemical analysis of Au single crystals: Stability of the UHV prepared surfaces of Au (111) and Au (100) in aqueous electrolyte." *Surface Science* 185.1-2 (1987): 88-104.

[49] Smith, C. I., et al. "Spectral signatures of the surface reconstructions of Au (110)/electrolyte interfaces." *Journal of Physics: Condensed Matter* 22.39 (2010): 392001.

[50] Kim, Jooho, Enrique Samano, and Bruce E. Koel. "Oxygen adsorption and oxidation reactions on Au (2 1 1) surfaces: Exposures using O2 at high pressures and ozone (O3) in UHV." *Surface science* 600.19 (2006): 4622-4632.

[51] Niehus, H. "Surface reconstruction of Cu (111) upon oxygen adsorption." *Surface Science* 130.1 (1983): 41-49.

[52] Bruch, L. W. "Theory of physisorption interactions." *Surface Science* 125.1 (1983): 194-217.

[53] Carneiro, K., et al. "Neutron-diffraction study of the solid layers at the liquid-solid boundary in He 4 films adsorbed on graphite." *Physical Review B* 24.3 (1981): 1170.

[54] Gangloff, Richard P., and Brian P. Somerday, eds. *Gaseous hydrogen embrittlement of materials in energy technologies: mechanisms, modelling and future developments*. Elsevier, 2012.

[55] Flanagan, Ted B., and W. A. Oates. "The palladium-hydrogen system." *Proceedings: EPRI-NSF Workshop on Anomalous Effects in Deuterided Metals*. 1991.

[56] Xu, Wei, et al. "Palladium catalyst immobilized on functionalized microporous organic polymers for C–C coupling reactions." *RSC advances* 9.59 (2019): 34595-34600.

[57] Adams, Brian D., and Aicheng Chen. "The role of palladium in a hydrogen economy." *Materials today* 14.6 (2011): 282-289.

[58] Wilke, Steffen, D. Hennig, and R. Löber. "Ab initio calculations of hydrogen adsorption on (100) surfaces of palladium and rhodium." *Physical Review B* 50.4 (1994): 2548.

[59] Felter, T. E., Erik C. Sowa, and M. A. Van Hove. "Location of hydrogen adsorbed on palladium (111) studied by low-energy electron diffraction." *Physical Review B* 40.2 (1989): 891.

[60] Han, Hyunsu, et al. "Plasma-induced oxygen vacancies in amorphous MnOx boost catalytic performance for electrochemical CO2 reduction." *Nano Energy* 79 (2021): 105492.

[61] Hoffmann F. M., “Infrared reflection-adsorption spectroscopy of adsorbed molecules,” Surface Science Reports, vol. 3, no. 2-3, pp. 107-192, 1983.

[62] Ozensoy, Emrah, Douglas C. Meier, and D. Wayne Goodman. "Polarization modulation infrared reflection absorption spectroscopy at elevated pressures: CO adsorption on Pd (111) at atmospheric pressures." *The Journal of Physical Chemistry B* 106.36 (2002): 9367-9371.

[63] O’Brien, Casey P., and Ivan C. Lee. "CO poisoning and CO hydrogenation on the surface of Pd hydrogen separation membranes." *The Journal of Physical Chemistry C* 121.31 (2017): 16864-16871.

[64] Solymosi, Frigyes, András Erdöhelyi, and Margit Lancz. "Surface interaction between H2 and CO2 over palladium on various supports." *Journal of Catalysis* 95.2 (1985): 567-577.

[65] Matsushima, Tatsuo. "Angular distribution of desorption of carbon dioxide produced on potassium-covered palladium (111) surfaces." *Journal of Physical Chemistry* 91.24 (1987): 6192-6197.

[66] Clarke, DEAN B., I. S. A. O. SUZUKI, and ALEXIS T. Bell. "An infrared study of the interactions of CO and CO2 with Cu/SiO2." *Journal of Catalysis* 142.1 (1993): 27-36.

[67] Fisher, Ian A., and Alexis T. Bell. "A comparative study of CO and CO2Hydrogenation over Rh/SiO2." *Journal of catalysis* 162.1 (1996): 54-65.

[68] Baiker, Alfons. "Utilization of carbon dioxide in heterogeneous catalytic synthesis." *Applied organometallic chemistry* 14.12 (2000): 751-762.

[69] Yang, Yixiong, et al. "Fundamental studies of methanol synthesis from CO 2 hydrogenation on Cu (111), Cu clusters, and Cu/ZnO (0001 [combining macron])." *Physical Chemistry Chemical Physics* 12.33 (2010): 9909-9917.

[70] Kattel, Shyam, Ping Liu, and Jingguang G. Chen. "Tuning selectivity of CO2 hydrogenation reactions at the metal/oxide interface." *Journal of the American Chemical Society* 139.29 (2017): 9739-9754.

[71] Carvajal, James, Guanrong Chen, and Haluk Ogmen. "Fuzzy PID controller: Design, performance evaluation, and stability analysis." *Information sciences* 123.3-4 (2000): 249-270.

[72] Borase, Rakesh P., et al. "A review of PID control, tuning methods and applications." *International Journal of Dynamics and Control* 9.2 (2021): 818-827.

[73] Shah, Pritesh, and Sudhir Agashe. "Review of fractional PID controller." *Mechatronics* 38 (2016): 29-41.

[74] M. A. Johnson and M. H. Moradi, PID control. Springer, 2005.

[75] Watts, John F., and John Wolstenholme. *An introduction to surface analysis by XPS and AES*. John Wiley & Sons, 2019.

[76] Siegbahn, Manne. "Relations between the K and L Series of the High-Frequency Spectra." *Nature* 96.2416 (1916): 676-676.

[77] Gilbert, Richard E., et al. "A method for rapid collection of high-energy-resolution Auger electron spectroscopy data: The digital-derivative-generation technique." *Journal of Vacuum Science & Technology A: Vacuum, Surfaces, and Films* 6.4 (1988): 2280-2286.

[78] Gilbert, Richard E., David F. Cox, and Gar B. Hoflund. "Computer-interfaced digital pulse counting circuit." *Review of Scientific Instruments* 53.8 (1982): 1281-1284.

[79] King, David A. "Thermal desorption from metal surfaces: A review." *Surface Science* 47.1 (1975): 384-402.

[80] Koitaya, Takanori, et al. "Observation of Fano line shapes in infrared vibrational spectra of CO2 adsorbed on Cu (997) and Cu (111)." *The Journal of Chemical Physics* 144.5 (2016): 054703.

[81] Redhead, P. A. "Thermal desorption of gases." *vacuum* 12.4 (1962): 203-211.

[82] "Chapter 4 structure and crystallography of adsorbed layers," in Adsorption on Methal Surfaces (J. Benard, Y. Berthier, F. Delarne, E. Hondros, M. Huber, P. Marcus, A. Masson, J. Oudar, and G. Rhead, eds.), vol. 13 of Studies in Surface Science and Catalysis, pp. 100-127, Elsevier 1983.

[83] De Broglie, Louis. "The wave nature of the electron." *Nobel lecture* 12 (1929): 244-256.

[84] E. McRae, "Surface crystallography: an introduction to low energy electron diffraction by lj clarke," Acta Crystallographica Section A: Foundations of Crystallography, vol. 42, no. 2, pp. 135–136, 1986.

[85] Gould, R. O. "Surface crystallography: an introduction to low energy electron diffraction by LJ Clarke." (1987): 224-224.

[86] Malik, N. H., A. A. Al-Arainy, and M. I. Qureshi. "FOUNDATIONS OF VACUUM SCIENCE AND TECHNOLOGY."

[87] Muttaqien, Fahdzi, et al. "CO2 adsorption on the copper surfaces: van der Waals density functional and TPD studies." *The Journal of Chemical Physics* 147.9 (2017): 094702.

[88] Argile, C., and G. E. Rhead. "Adsorbed layer and thin film growth modes monitored by Auger electron spectroscopy." *Surface Science Reports* 10.6-7 (1989): 277-356.

[89] Baskaran, Arvind, and Peter Smereka. "Mechanisms of stranski-krastanov growth." *Journal of Applied Physics* 111.4 (2012): 044321.

[90] Evans, M. M. R., J. C. Glueckstein, and J. Nogami. "Epitaxial growth of manganese on silicon: Volmer-Weber growth on the Si (111) surface." *Physical Review B* 53.7 (1996): 4000.

[91] Thornton, John A. "High rate thick film growth." *Annual review of materials science* 7.1 (1977): 239-260.

[92] Sandell, Anders, and Alexander J. Jaworowski. "The Mn 2p core-level photoelectron spectrum of Pd–Mn bimetallic systems on Pd (1 0 0)." *Journal of electron spectroscopy and related phenomena* 135.1 (2004): 7-14.

[93] Strohmeier, Brian R., and David M. Hercules. "Surface spectroscopic characterization of manganese/aluminum oxide catalysts." *The Journal of Physical Chemistry* 88.21 (1984): 4922-4929.

[94] Biesinger, Mark C., et al. "Resolving surface chemical states in XPS analysis of first row transition metals, oxides and hydroxides: Cr, Mn, Fe, Co and Ni." *Applied Surface Science* 257.7 (2011): 2717-2730.

Appendix A

Data

XPS of Mn 2 $p_{3/2}$ can be seen in Figure A.2 for 1.5 ML of MnO_x thin films created at room and liquid nitrogen temperature. Both films were created by heating the Mn source with 15 A of DC. The heated Mn sample can be seen in Figure A.1.

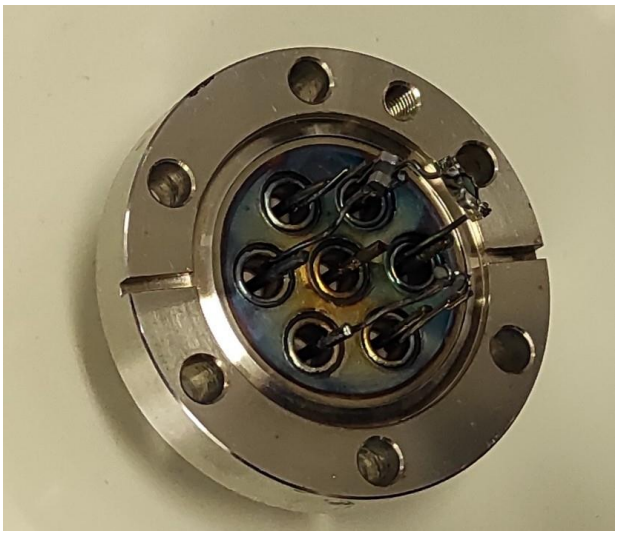

Figure A.1: Mn sources can be seen on the picture

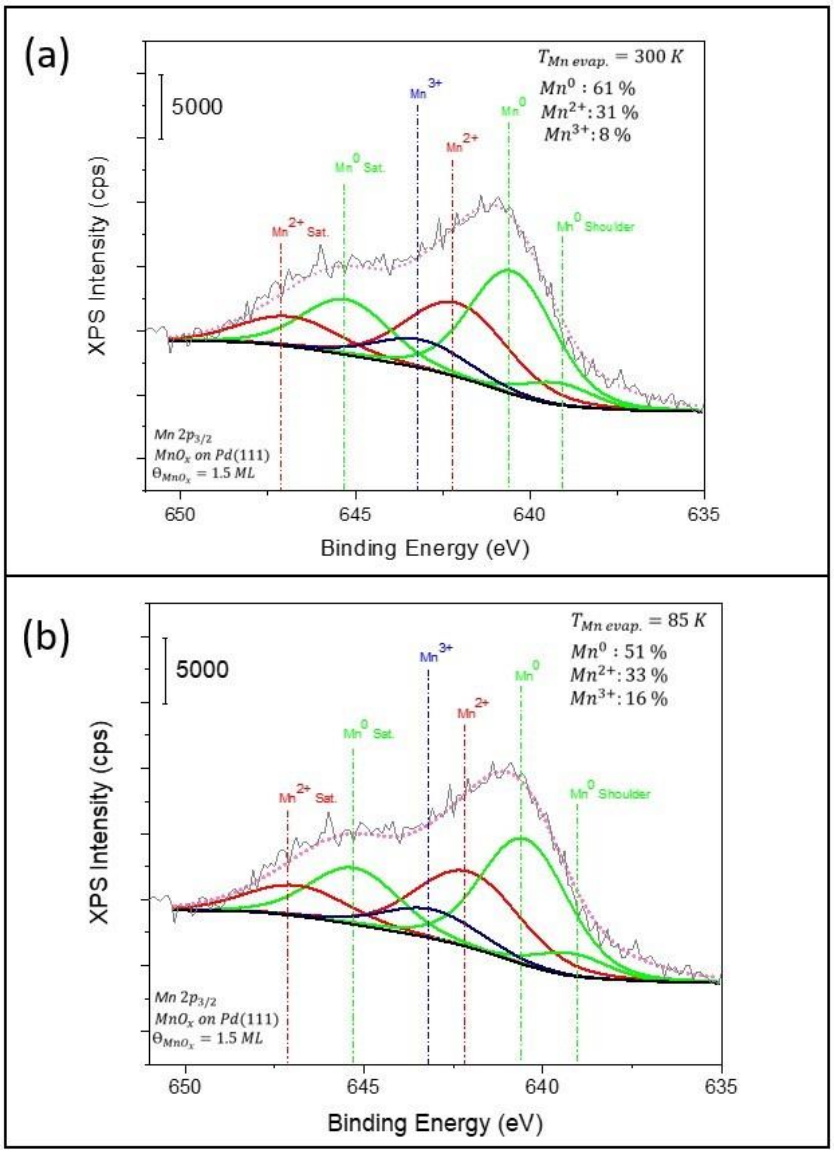

Figure A.2: (a) Mn 2 $p_{3/2}$ 1.5 ML MnO_x thin film formed at room temperature (b) 85 K

Appendix B

Experimental

B.1 Adjustment of PID Controller

PC 771 PID controller is adjusted by using auto-tune property. However, auto-tune is ineffective in determining the P, I, and D parameters for a linear heat. After a few trials of the auto-tune, relatively close P, I, and D parameters are adjusted by the device, but adjustment may not provide linear heating for a 1 cm diameter of a single crystal sample. Therefore, manual adjustment for the P, I, and D parameters are required. It should be noted that P, I, and D parameters should be adjusted, respectively. If the PID parameters are not set in order, you must repeat the auto-tune process a few times and return to the starting point. Moreover, different samples can require different P, I, and D parameters due to their different mass and heat capacitance for the Pd(111) single crystal with 1 cm diameter. P, I, and D parameters were adjusted as 320, 80, and 1.0, respectively.

There are two main adjustment parts for the Ordel PC 771. If you spontaneously press and hold the * and curved arrow, which is the button at the right of the stop button, you can reach the C1 and C2 parts. C1 is used to make adjustments for the P, I, D, and other parameters, including offset. (Current offset value was adjusted as -4.2 to measure the correct liquid nitrogen temperature of the sample.) If the values on the C1 are enough to make linear heating, I strongly

recommend any change in this part. If you push the bottoms * and curved arrow, you can reach the programming part of the heating. You can write eight different programs for heating. For each program, especially for the TPD, an adjustment of the starting point, -188 ºC, should be written before the program is used. If you do not type this value before a TPD experiment, you can see a serious deviation from the linear heating. Currently, Program 1, 2, 3, 4, and 5 is used for the TPD experiment (from 85 K to 800 K), annealing at 800 ºC, Flashing, and constant temperature at 85 K and room temperature, respectively.

If you remove the sample or make a new thermocouple connection by spot welding, DO NOT forget to remove ALL connections of the PID controller. Without removing the cables of the PID controller, when you make a spot welding, the current you applied will also pass from the PID controller and burn it.

If the PID controller is broken. You can order a new one from Ordel. Current PID controller properties can be seen in Figure B.1. All Ordel PC 771, do not have the same properties. Especially, all outputs are adjusted by the customer's needs. If one of the parts or parts were broken, repairing might not be possible.

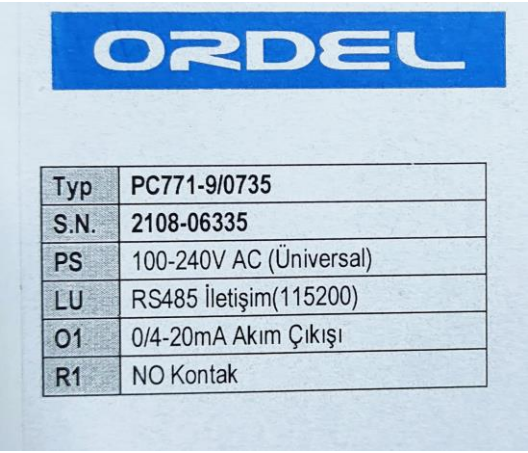

Figure B.1: Properties of current PID controller. Ordel PC 771